Combining MRI blood flow data with one-dimensional blood flow models to perform patient-specific noninvasive pressure prediction

David Hamel

BSc. Thesis Applied Mathematics and Applied Physics

Supervisors

Dr. S. Kenjeres

Prof. dr. ir. C. Vuik

Delft University of Technology
Delft
June 2020

Abstract

In this thesis, the behaviour and application of a one-dimensional model describing blood flow through compliant vessels is investigated. The one-dimensional model is derived using the physical laws of conservation of momentum and conservation of mass and uses a Finite Volume Method in combination with a high resolution flux difference splitting. First, the behaviour of the model is compared with established models in a network of 55 main arteries and then in a network of 111 main arteries including *in vivo* results. Finally, the model with the 111-artery network as a baseline is combined with inflow boundary conditions and a scaling factor provided by MRI blood flow data to make it patient-specific. The adapted model is used to investigate how well characteristics in the distal part of the network can be predicted. It is found that the Finite Volume Method in combination with the high resolution flux difference splitting produces results that are highly comparable to those of established models both in the 55- and 111-artery network. The patient-specific model proves to be capable of predicting the pressure value in the arm to a reasonable degree. The flow in distal parts in the aorta is underestimated for all patients, but the degree of this underestimation varies per patient. Combining the results with a novel colour representation of pressure and velocity, it is possible to show patient specific evolution of pressure and velocity in their arteries. Further research should focus on adapting baseline networks with different key characteristics to increase the accuracy of the predictions for patients with different characteristics than the baseline model used in this study. Such characteristics include the number of bifurcations in the aortic arch (three or two) and the tapering of the aorta.

Contents

1 Introduction

Investigating the workings of the human body has always been difficult. The underlying mechanisms are incredibly complex and often have millions or even billions of individual components all working together. Moreover, ethical concerns make *in vivo* research very difficult. Our ever increasing computational power might solve both these problems at once. We are constantly pushing boundaries of the complexity of models describing the systems of the human body. These models simultaneously make it possible to investigate and diagnose with minimal surgical risk.
In developed countries cardiovascular diseases are responsible for as much as 20-25% of annual deaths. This makes researching the workings of the blood circulation of incredible value. Ideally, a patient specific model of the blood circulation can help make potentially life-saving decisions if a medical expert is interested in the cardiovascular state of a patient. There are two big problems to developing patient specific models. First is the still formidable computational time when using 3D models based on the Navier-Stokes equations. Second is the lack of enough patient specific data to comprise a detailed enough model. Under reasonable circumstances, a simplified one-dimensional model can be used to immensely cut computational time whilst enjoying highly comparable results to 3D models Mynard [4]. Using a baseline network that is scaled for each individual patient could reduce the amount of parameters needed to estimate for a patient from hundreds to a handful.
The aim of this thesis consists of two parts. First, we will further develop the Finite Volume Method developed in Rozendaal [7] and investigate its performance. Secondly, we will use data from the Leids Universitair Medisch Centrum (LUMC) retrieved with a MRI scan to investigate the possibility of scaling a baseline method to produce partially patient-specific models.
First, as recommended by [7] we will change the treatment of bifurcations to achieve more realistic results when dealing with arterial trees. We will then investigate results obtained when simulating an arterial network of 55 arteries.
Next, the model will be expanded. Inflow and outflow boundary conditions from the original model will be changed to be more in alignment with literary standards. Again the behaviour of the Finite Volume Method will be investigated. The results will be compared to results obtained in literature and *in vivo* measurements.
Finally, we will investigate the use of a baseline model and MRI data to make a partially patient-specific model. The 111-artery network is used as a baseline network. The flow data from the MRI scan will be used as an inflow boundary condition and the model will be scaled to be in agreement with measurements of the cross-sectional area of the aorta by the MRI. Two scaling methods are researched. A simple single-factor scaling method and a more complicated multi-factor scaling. Flow data in distal parts of the aorta and pressure measurements in the left and right arm will be used to investigate performance. We will simultaneously research if the model is capable of making reasonable predictions and which scaling method is preferred.
This thesis is structured as follows. First, a summary of the current work in the field of one-dimensional models of blood flow is given.
Then, the mathematical basis for the model is given in sections 3-6. Sections 3-5 concern the derivation of the model and numerical method which was already covered in [7] and we will provide for completeness. Conservation of mass and momentum is used to derive the equations that describe blood flow in compliant vessels. After this, the equations are transformed into the characteristic equations that provide important insight into the workings of the model. The numerical method is subsequently described. Following this, several methods to model the circulation, for example a model for a heart, are presented and discussed. This concludes the mathematical basis.
We continue with the validation of the model in sections 7-8. The 55-artery network results are discussed and are followed by the discussion of the 111-artery network results. This concludes the validation of the model.
The making of a partially patient-specific model is discussed and its performance investigated in section 9. This section contains many novel implementations of one-dimensional models. Finally, conclusions about the performance of the Finite Volume Method and the method of creating partially patient-specific models are drawn.

2 Literature survey

A short summary containing the current work of one-dimensional models of the human vascular system.
A system of Partial Differential Equations (PDEs) can be derived using the conversation of mass and momentum. There are two general forms of this system of PDEs, one based on the volumetric flow Q and mean velocity u and another one based on the cross-sectional area A and u. The two forms are equivalent for smooth solutions. For discontinuous solutions then the form with Q and u is the proper form, see Sherwin et al. [15]. Thus this is the form we will use. Under normal physiological conditions, the solutions remains smooth.
The system must be completed by a relation between pressure p and the cross-sectional area A. Several relationships have been proposed, for a list see Mynard [4]. We will use the relationship adopted in [2, 3, 4, 15]. This relationship requires an estimation of the stiffness of the artery. This can be done experimentally or by using the formula proposed by Olufsen [9].
Bifurcations, or more generally branching points, are treated by solving a nonlinear system of equations consisting of continuation of the characteristic variables, pressure and the conservation of mass. The system is solved using the Newton-Raphson method, see [4, 5, 15]. We will adopt the same treatment.
There have been many models of the heart. Some are part of a closed loop model as in Mynard and Smolich [10]. We will use the model used in Sherwin [15] when dealing with the 55-artery model and the model proposed by [4] when dealing with the 111-artery network.
Due to the high complexity of the human arterial network, it has to be truncated at a certain point. This is done by using an outflow boundary condition. In the 55-artery network, a reflection coefficient is used as in Sherwin et al. [15]. In the 111-artery a windkessel model is used. The windkessel model is a 0D analogy from electrical circuits and was first used in [11]. It is the most used outflow boundary condition and is used in [2, 3, 16], a variant that is suitable for closed-loop models is used in [10].
In literature, Finite Elements Methods (FEM) are often used such as the Taylor Galerkin scheme or the Discontinuous Galerkin. We will thus use the FEM schemes as a way of validating our Finite Volume Method (FVM) approach.
Bale and LeVeque [1] describe a Finite Volume Method that is designed for spatially varying flux functions.
The application of one-dimensional blood flow models has mostly focused on simulating various diseased states. For example Sherwin et al. [15] studied the effect of implanted stents, Fossan et al. [3] studied the effect of a stenosis (a narrowing of the blood vessel). For more applications, a comprehensive summary is given in Malatos et al. [8]. Most applications focus on a more general analysis of a diseased state and are not patient-specific, they mostly offer only qualitatively accurate results but still offer important clinical insight.
Although the flow at the beginning of the Ascending Aorta has been used as an inlet boundary condition in [16], we are not aware of the coupling of MRI scans with MRI data to produce partially patient-specific models.

3 Derivation of the model

We begin with the mathematical basis by deriving the basic one-dimensional flow model. We model blood vessels as being composed of strictly circular cross-sections with the x axis serving as the cylindrical axis. The velocity profile is assumed to be flat. The area of the cross-section is given by $A(x,t)$. The mean velocity across a cross-section is denoted by $u(x,t)$. A schematic overview of a blood vessel is given in Figure 1.

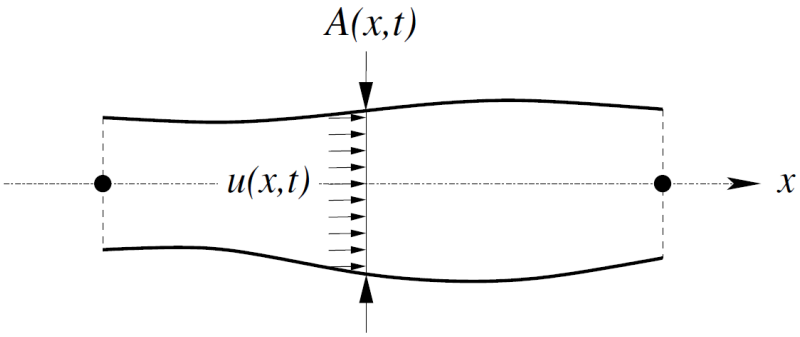

Figure 1: Schematic overview of a blood vessel with A and u from Peiró et al. [12].

3.1 Conservation of mass

We consider a control volume from $x = a$ to $x = b$. The mass in this control volume is given by $\int_a^b \rho(x,t)A(x,t)dx$. Here $A(x,t)$ is the area of a cross-section at position x and time t in m^2 and $\rho(x,t)$ in $\mathrm{kg/m}^3$. Blood is modelled as an incompressible fluid, $\rho(x,t) = \rho = 1021\mathrm{kg/m}^3$. Now the change of the mass in the control volume is dependent on how much mass flows in at the interface at $x = a$ and how much flows out at $x = b$ per unit time. This flow is known as the mass flux. The mass flux at $x = a$ is given by $\rho A(a,t)u(a,t)$, the mass flux at $x = b$ is given by $\rho A(b,t)u(b,t)$. Here $u(x,t)$ is given in $\mathrm{m/s}$. We can therefore write

$$\frac{d}{dt}\int_a^b \rho A dx = \rho A(a,t)u(a,t) - \rho A(b,t)u(b,t) \tag{1}$$

It is reasonable under normal conditions to assume that A and u are sufficiently smooth. The right-hand side can be rewritten as

$$\rho A(a,t)u(a,t) - \rho A(b,t)u(b,t) = -\rho \int_a^b \frac{\partial (Au)}{\partial x} dx \tag{2}$$

Since ρ is independent of time we can combine equation (1) and (2) to give

$$\rho \int_a^b \frac{\partial A}{\partial t} + \frac{\partial Au}{\partial x} dx = 0 \tag{3}$$

The generality of this equation allows us to state that

$$\frac{\partial A}{\partial t} + \frac{\partial Au}{\partial x} = 0 \tag{4}$$

This is the first equation of the general model.

3.2 Conservation of momentum

We again use the control volume from $x = a$ to $x = b$. The conservation of momentum tells us that the only way momentum inside the control volume, given by $\int_a^b \rho A u dx$, can change is through the momentum flux at the boundaries, given by $\rho A(a,t)u(a,t)^2$ and $\rho A(b,t)u(b,t)^2$ respectively, and applied forces F. Thus

$$\frac{d}{dt}\int_a^b \rho A u dx = \rho A(a,t)u(a,t)^2 - \rho A(b,t)u(b,t)^2 + F \tag{5}$$

The forces F consist of several forces. First the body forces, which we assume to be zero. Secondly, the surface forces at the boundary given by $A(a,t)p(a,t) - A(b,t)p(b,t)$ where $p(x,t)$ denotes the pressure at x and t in Pa. The side wall pressure force, $\int_a^b p\frac{\partial A}{\partial x}dx$ and a viscous resistance force, $-\int_a^b 2\pi R\tau dx$. Here $\tau = \mu(\frac{\partial u}{\partial r})|_R$ is the shear stress, $\mu \approx 0.035\ P$ is the viscosity, r is the radial direction and R is the vessel radius. This leads to

$$F = A(a,t)p(a,t) - A(b,t)p(b,t) + \int_a^b p\frac{\partial A}{\partial x}dx - \int_a^b 2\pi R\tau dx \tag{6}$$

Combining equations (5) and (6) and rewriting the boundary terms as integrals, we get

$$\rho\int_a^b \frac{\partial Au}{\partial t}dx = -\rho\int_a^b \frac{\partial Au^2}{\partial x}dx - \int_a^b \frac{\partial Ap}{\partial x}dx + \int_a^b p\frac{\partial A}{\partial x}dx - \int_a^b 2\pi R\tau dx \tag{7}$$

Simplifying yields

$$\rho\int_a^b (\frac{\partial Au}{\partial t} + \frac{\partial Au^2}{\partial x} + \frac{1}{\rho}\frac{\partial Ap}{\partial x} - \frac{p}{\rho}\frac{\partial A}{\partial x} + \frac{1}{\rho}2\pi R\tau)dx = 0 \tag{8}$$

Again, generality leads to the conclusion that

$$\frac{\partial Au}{\partial t} + \frac{\partial Au^2}{\partial x} + \frac{1}{\rho}\frac{\partial Ap}{\partial x} - \frac{p}{\rho}\frac{\partial A}{\partial x} + \frac{1}{\rho}2\pi R\tau = 0 \tag{9}$$

Making use of the product rule for differentiation,

$$\frac{\partial Au}{\partial t} = \frac{\partial A}{\partial t}u + \frac{\partial u}{\partial t}A,\ \frac{\partial Au^2}{\partial x} = \frac{\partial Au}{\partial x}u + \frac{\partial u}{\partial x}Au,\ \frac{\partial Ap}{\partial x} = \frac{\partial A}{\partial x}p + \frac{\partial p}{\partial x}A \tag{10}$$

we can simplify equation (9) to

$$A(\frac{\partial u}{\partial t} + u\frac{\partial u}{\partial x} + \frac{1}{\rho}\frac{\partial p}{\partial x} + \frac{1}{\rho}\frac{2}{R}\tau) + (\frac{\partial A}{\partial t} + \frac{\partial Au}{\partial x}) = 0 \tag{11}$$

Now the last term equals zero due to the conservation of momentum. Flow in the major arteries is often considered to be laminar and the expression for Poiseuille flow, which is fully developed ($\frac{\partial u}{\partial x} = 0$) and steady ($\frac{\partial u}{\partial x} = 0$) is

$$\tau = -\frac{R}{2}\frac{dp}{dx} = \frac{R}{2}\frac{8\mu Q}{\pi R^4} = \frac{R}{2}\frac{8\pi\mu u}{A} \tag{12}$$

This does not hold for turbulent flow or non-Newtonian flow. Note that assuming Poiseuille flow means assuming a parabolic velocity profile. With this assumption we arrive at

$$\frac{\partial u}{\partial t} + u\frac{\partial u}{\partial x} + \frac{1}{\rho}\frac{\partial p}{\partial x} + \frac{8\pi\mu u}{A\rho} = 0 \tag{13}$$

3.3 The final system

To complete the system of equations, we assume a relationship between the pressure of a blood vessel and its cross-sectional area. This relationship is the same as in Sherwin et al. [15], given by

$$p = p_{\text{ext}} + \beta(\sqrt{A} - \sqrt{A_0}) \tag{14}$$

Where p_{ext} is the external pressure in Pa, $A_0(x)$ is the cross-sectional area in m^2 in equilibrium. β is given by

$$\beta = \frac{\sqrt{\pi} h_0 E}{(1-\nu^2)A_0} \tag{15}$$

Here $E(x)$ is the Young modules in Pa, h_0 is the vessel thickness at equilibrium $(p, u) = (p_{\text{ext}}, 0)$. ν is the Poisson ratio, for biological tissue it is most commonly taken as $\nu = \frac{1}{2}$.
For the 55-artery model, the values of β have been experimentally determined and those values will be used. For the 111 artery model, we will use the empirical formula suggested by Olufsen [9] to determine h_0 and E

$$c_0^2 = \frac{2}{3\rho}\frac{Eh_0}{r_0} = \frac{2}{3\rho}[k_1 \exp(k_2 r_0) + k_3] \tag{16}$$

Where c_0 and r_0 are the pulse wave velocity and radius of the vessel at rest. The values of k_1, k_2 and k_3 are set to $3 \cdot 10^6$ g s^{-2} cm^{-1}, -9 cm^{-1} and $33.7 \cdot 10^4$ g s^{-2} cm^{-1} respectively.

3.4 Conservative form

Now that we have derived the system (non-linear) partial differential equations given by

$$\begin{cases} \frac{\partial A}{\partial t} + \frac{\partial Au}{\partial x} = 0 \\ \frac{\partial u}{\partial t} + u\frac{\partial u}{\partial x} + \frac{1}{\rho}\frac{\partial p}{\partial x} + 8\pi\mu\frac{u}{A\rho} = 0 \end{cases} \tag{17}$$

completed by

$$p = p_{\text{ext}} + \beta(\sqrt{A} - \sqrt{A_0})$$

We want to write the system in a conservative form, so that it is better to handle. To that end, we write

$$U = \begin{bmatrix} A \\ u \end{bmatrix}, \quad F(U) = \begin{bmatrix} Au \\ \frac{1}{2}u^2 + \frac{p}{\rho} \end{bmatrix}, \quad S(U) = \begin{bmatrix} 0 \\ -8\pi\mu\frac{u}{A\rho} \end{bmatrix} \tag{18}$$

So that the system of equations can be written as

$$\frac{\partial U}{\partial t} + \frac{\partial F(U)}{\partial x} = S(U) \tag{19}$$

Where U is the conserved quantity, $F(U)$ is the flux function and $S(U)$ denotes the source term. If we integrate equation (19) from $x = a$ to $x = b$, we see why it is known as the conservative form

$$\int_a^b \frac{\partial U}{\partial t} dx + \int_a^b \frac{\partial F(U)}{\partial x} dx = \int_a^b S(U) dx \tag{20}$$

If U is sufficiently smooth, this leads to

$$\frac{\partial}{\partial t}\int_a^b U dx = F(U)|_a - F(U)|_b + \int_a^b S(U) dx \tag{21}$$

Here we recognise that U is a conserved quantity in a control volume from a to b. It can only change in time through the fluxes through the boundaries $F(U)$ and/or the source function $S(U)$ that acts within the control volume.

4 Characteristic equations

Our goal is now to describe the nonlinear system of partial differential equations we derived earlier using a system of characteristic equations. These equations, supplemented with the required characteristic variables, should describe the behaviour of the nonlinear system fully. An advantage of these characteristic equations is that they provide meaningful insights into how the system works. They are also of interest when setting boundary conditions for the system.

4.1 Derivation of the characteristic equations

Whilst deriving the characteristic equations, we assume $p_{\text{ext}} = 0$, $\beta = \beta(x)$ and $A_0 = A_0(x)$. Applying the chain rule to equation (14)

$$\frac{\partial p}{\partial x} = \frac{\partial p}{\partial A}\frac{\partial A}{\partial x} + \frac{\partial p}{\partial \beta}\frac{\partial \beta}{\partial x} + \frac{\partial p}{\partial A_0}\frac{\partial A_0}{\partial x} = \frac{\beta}{2\sqrt{A}}\frac{\partial A}{\partial x} + (\sqrt{A} - \sqrt{A_0})\frac{\partial \beta}{\partial x} - \frac{\beta}{2\sqrt{A_0}}\frac{\partial A_0}{\partial x} \tag{22}$$

This result is now substituted into the system of partial differential equations (19) and the chain rule is once more applied to arrive at a quasi-linear form

$$\frac{\partial U}{\partial t} + H(U)\frac{\partial U}{\partial x} = \begin{bmatrix} A \\ u \end{bmatrix}_t + \begin{bmatrix} u & A \\ \frac{\beta}{2\rho\sqrt{A}} & u \end{bmatrix}\begin{bmatrix} A \\ u \end{bmatrix}_x = K(U) \tag{23}$$

Where $K(U)$ is defined by

$$K(U) = \begin{bmatrix} 0 \\ -8\pi\mu\frac{u}{A\rho} - \frac{1}{\rho}\left\{(\sqrt{A} - \sqrt{A_0})\frac{\partial \beta}{\partial x} - \frac{\beta}{2\sqrt{A_0}}\frac{\partial A_0}{\partial x}\right\} \end{bmatrix} \tag{24}$$

The Jacobian of the flux function is given by

$$H(U) = \frac{\partial F(U)}{\partial U}\begin{bmatrix} u & A \\ \frac{\beta}{2\rho\sqrt{A}} & u \end{bmatrix} \tag{25}$$

The eigenvalues of $H(U)$ are found to be $\lambda_\pm = u \pm c$. Here c is the velocity of a wave when the fluid is at rest and is know as the basic wave speed and is given by $c = \sqrt{\frac{\beta}{2\rho}}A^{1/4}$. If the fluid is not at rest, the waves are travelling at $\lambda_\pm = u \pm c$.
As was found in [15], normal physiological conditions result in $c > u$. Thus the system consists of waves running forward at a speed of $\lambda_+ = u + c$, and waves running backward at $\lambda_- = u - c$. Furthermore the eigenvalues are real and distinct, and the system is strictly hyperbolic.
Diagonalizing H yields

$$H = R\Lambda R^{-1} = \begin{bmatrix} \frac{A}{2c} & -\frac{A}{2c} \\ \frac{1}{2} & \frac{1}{2} \end{bmatrix}\begin{bmatrix} u+c & 0 \\ 0 & u-c \end{bmatrix}\begin{bmatrix} \frac{c}{A} & 1 \\ -\frac{c}{A} & 1 \end{bmatrix} \tag{26}$$

Substituting this into equation (23) and rewriting results in

$$R^{-1}\frac{\partial U}{\partial t} + \Lambda R^{-1}\frac{\partial U}{\partial x} = R^{-1}K(U) \tag{27}$$

The system is now rewritten in terms of the characteristic variables $W = \begin{bmatrix} w_1 \\ w_2 \end{bmatrix}$. To this end we implicitly define W such that $\frac{\partial W}{\partial U} = R^{-1}$. Thus

$$\frac{\partial(w_1, w_2)}{\partial(A, u)} = \begin{bmatrix} \frac{\partial w_1}{\partial A} & \frac{\partial w_1}{\partial u} \\ \frac{\partial w_2}{\partial A} & \frac{\partial w_2}{\partial u} \end{bmatrix} = \begin{bmatrix} \frac{c}{A} & 1 \\ -\frac{c}{A} & 1 \end{bmatrix} \tag{28}$$

From this we can derive the expressions of the characteristic variables. They are given by

$$w_1 = u + 4c = u + 4A^{1/4}\sqrt{\frac{\beta}{2\rho}}, \quad w_2 = u - 4c = u - 4A^{1/4}\sqrt{\frac{\beta}{2\rho}} \tag{29}$$

Inverting the expressions yields

$$A = \left(\frac{w_1 - w_2}{4}\right)^2 \left(\frac{\rho}{2\beta}\right)^2, u = \frac{w_1 + w_2}{2} \tag{30}$$

Substituting the expression for R^{-1} into equation (27)

$$\frac{\partial W}{\partial U}\frac{\partial U}{\partial t} + \Lambda\frac{\partial W}{\partial U}\frac{\partial U}{\partial x} = R^{-1}K(U) \tag{31}$$

The chain rule is used to state

$$\frac{\partial W}{\partial t} = \frac{\partial W}{\partial U}\frac{\partial U}{\partial t} \tag{32}$$

and for the spacial derivative

$$\frac{\partial W}{\partial x} = \frac{\partial W}{\partial U}\frac{\partial U}{\partial x} + \frac{\partial W}{\partial \beta}\frac{\partial \beta}{\partial x} \Longrightarrow \frac{\partial W}{\partial U}\frac{\partial U}{\partial x} = \frac{\partial W}{\partial x} - \frac{\partial W}{\partial \beta}\frac{\partial \beta}{\partial x} \tag{33}$$

We can use this identities to write the system as

$$\frac{\partial W}{\partial t} + \Lambda\frac{\partial W}{\partial x} = R^{-1}K + \Lambda\frac{\partial W}{\partial \beta}\frac{\partial \beta}{\partial x} \tag{34}$$

Using the relations in (30) we can write this equation completely in terms of w_1 and w_2, thus completing the transformation.
If we assume inviscid flow, $\mu = 0$ P, and look at regions where the elasticity and the cross-sectional area are not space-dependent, $\beta(x) = \beta$ and $A_0(x) = A(x)$, the equation can be simplified even further.

$$\frac{\partial W}{\partial t} + \Lambda\frac{\partial W}{\partial x} = 0 \tag{35}$$

or component wise

$$\frac{\partial w_1}{\partial t} + \lambda_1\frac{\partial w_1}{\partial x} = 0, \quad \frac{\partial w_2}{\partial t} + \lambda_2\frac{\partial w_2}{\partial x} = 0 \tag{36}$$

Noting that $\lambda_+ = u + c = \frac{w_1+w_2}{2} + \sqrt{\frac{\beta}{2\rho}}\frac{w_1-w_2}{4}\sqrt{\frac{\rho}{2\beta}} = \frac{5w_1+3w_2}{8}$ and $\lambda_- = \frac{3w_1+5w_2}{8}$, we have arrived at a coupled system of quasi-linear Partial Differential Equations. If we assume $\lambda_\pm$ to be constant, the solution consists of two transport equations where the velocity is given by $\lambda_\pm$.

The transformation of the original system of PDEs into the characteristic equations with characteristic variables w_1 and w_2 shows that throughout the domain of the system information is carried by w_1 in the positive direction and by w_2 in the negative direction. This important insight will be used to state boundary conditions and handle the branching of arterial networks.

5 Numerical Method

We will now describe the numerical method used to evaluate the system of nonlinear PDEs. We begin by assuming the frictional force to be small and negligible. Thus we set μ to zero in equation (18). This results in

$$\frac{\partial U}{\partial t} + \frac{\partial F(U,x)}{\partial x} = 0, U = \begin{bmatrix} A \\ u \end{bmatrix}, \quad F(U,x) = \begin{bmatrix} Au \\ \frac{1}{2}u^2 + \frac{p}{\rho} \end{bmatrix} \tag{37}$$

The system (37) is strictly Hyperbolic. Hyperbolic PDEs are often found describing wave propagation and transport phenomena. They are closely related to conservation laws. In fact, the current system of PDEs was derived using the conservation of mass and momentum. It thus makes sense to pick a scheme that naturally has the property of satisfying these conservation laws. Finite Volume Methods (FVM) have this property and thus seem a natural choice to describe our system of PDEs.

5.1 Stability

As we are dealing with a hyperbolic PDE, the CFL condition must be met to ensure stability in the time domain. The condition for the time step that follows from the CFL condition is

$$\Delta t \leq \frac{\Delta x}{|\lambda_i|}, \quad i \in \{1, 2\} \tag{38}$$

In this case, the CFL condition can be interpreted as ensuring that waves originating at cell interfaces can only influence the bordering cells. This can be seen from $s = |\lambda_i| \, \Delta t \leq \Delta x$.

5.2 Linear case

To better understand how to use FVM methods for this nonlinear problem, we first look at a linear case. This test case only serves the purpose of inspiring our approach to the original problem and the variables have no physical meaning.

$$\frac{\partial q}{\partial t} + A\frac{\partial q}{\partial x} = \begin{bmatrix} q_1 \\ q_2 \end{bmatrix}_t + \begin{bmatrix} a & b \\ b & a \end{bmatrix} \begin{bmatrix} q_1 \\ q_2 \end{bmatrix}_x = \begin{bmatrix} 0 \\ 0 \end{bmatrix} \tag{39}$$

Since A is symmetric, it has two distinct real eigenvalues if $b \neq 0$. It then is strictly hyperbolic. To solve this linear case with an FVM method, we discretize the domain in equidistant intervals (volumes) of Δx as in LeVeque [13]. Each individual cell, C_i is centered around x_i and is given by $(x_i - \frac{1}{2}\Delta x, x_i + \frac{1}{2}\Delta x)$. We denote the average value of Q in C_i at time n by $Q_i^n = \frac{1}{\Delta x}\int_{C_i} Q(x, t^n)dx$. For this average we use the following scheme

$$Q_i^{n+1} = Q_i^n - \frac{\Delta t}{\Delta x}\left(A^+ \Delta Q_{i-1/2}^n + A^- \Delta Q_{i+1/2}^n\right) \tag{40}$$

In this equation, $A^{\pm}\Delta Q_{i\mp 1/2}^n$ represent the fluctuations through the boundaries of x_i. $A^+\Delta Q_{i-1/2}^n$ represents the effect of all right flowing waves at the left boundary of C_i, namely $x_{i-1/2}$. In the same way $A^-\Delta Q_{i+1/2}^n$ represents all left flowing waves at the right boundary, $x_{i+1/2}$. Thus if there is no net inflow or outflow, Q_i does not change with time, as is expected when inspecting system (39) as there is no source term. When A is diagonalized as $A = R\Lambda R^{-1}$, we can calculate the fluctuations with

$$\begin{aligned} A^+\Delta Q_{i-1/2}^n &= R\Lambda^+ R^{-1}\left(Q_i^n - Q_{i-1}^n\right) \\ A^-\Delta Q_{i+1/2}^n &= R\Lambda^- R^{-1}\left(Q_{i+1}^n - Q_i^n\right) \end{aligned} \tag{41}$$

Here $\Lambda^{\pm}$ are given by

$$\mathbf{\Lambda}^+ = \begin{bmatrix} \lambda_1 & 0 \\ 0 & 0 \end{bmatrix}, \quad \mathbf{\Lambda}^- = \begin{bmatrix} 0 & 0 \\ 0 & \lambda_2 \end{bmatrix} \tag{42}$$

5.3 Riemann problem

Since we are dealing with a nonlinear problem, we can not use the numerical scheme in (40) combined with (41) and (42) directly. However, we can use the general method of solving for the next time-average by using the inflow and outflow through the two boundaries of a cell. We will thus investigate how the time average changes as a function of these inflows and outflows for our nonlinear problem. To this end we investigate the Riemann problem.

The Riemann problem is an initial value problem of a conservation law with piece wise constant initial data and a single discontinuity. The goal is to understand how the solution behaves as a function of the discontinuity at the boundaries of cells. When this is known, the scheme of (40) can be adapted to solve for the entire domain.

We study the situation on the interface of cell *i* and cell *i* -1. For the initial data we choose at time t^n

$$U(x,t^n) = \begin{cases} U_{i-1}^n, & x < x_{i-1/2} \\ U_i^n, & x > x_{i-1/2} \end{cases} \tag{43}$$

Here $x_{i-1/2}$ is the border between the two cells. We will use a couple of linearizations to simplify the problem and to approximate the cell averages at t^{n+1}.
First we approximate the flux function $F(U,x)$ as being constant in each cell. The value of this discretized flux function is determined at the center of the cell, for cell C_i this is the point x_i. We write $F_i(U) = F(U,x_i)$.
The solution for the Riemann problem now splits into two domains

$$\begin{aligned} \frac{\partial U}{\partial t} + \frac{\partial F_{i-1}(U)}{\partial x} &= 0, \quad \text{if } x < x_{i-1/2} \\ \frac{\partial U}{\partial t} + \frac{\partial F_i(U)}{\partial x} &= 0, \quad \text{if } x > x_{i-1/2} \end{aligned} \tag{44}$$

This solution is only valid for $x \in (x_{i-3/2}, x_{i+1/2})$ due to the CFL condition. To better understand the behaviour of the solution, the domain is represented in Figure 2. On the y-axis we see the evolution of time from t^n to t^{n+1}. On the x-axis we see the two cells C_{i-1} and C_i and their interface at $x_{i-1/2}$. At any point in time, the x-coordinate of the tilted lines tells us how far the information from the interface has travelled. Thus the value of U is constant in all enclosed volumes.

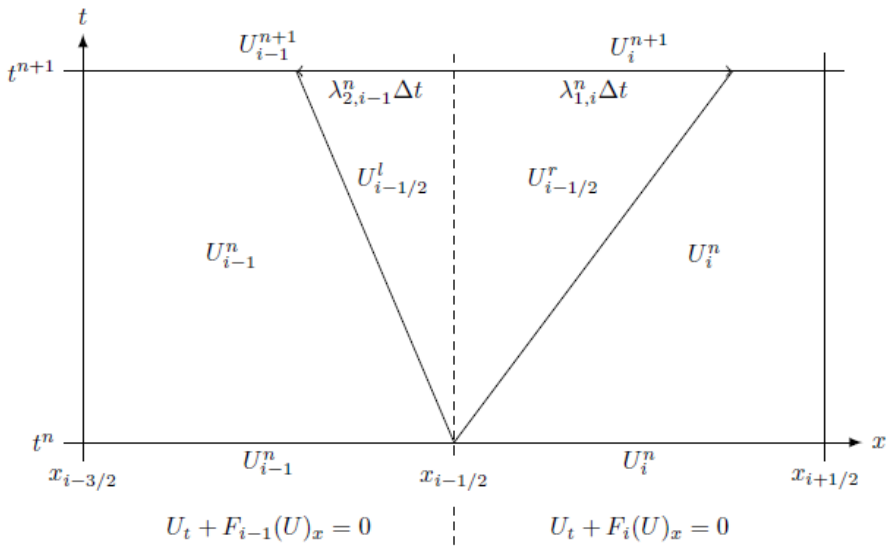

Figure 2: Domain of the Riemann problem solution, from [7].

For bounded solutions we expect the flux to be conserved across the cells interface at $x_{i-1/2}$.

$$F_{i-1}(U^l_{i-1/2}) = F_i(U^r_{i-1/2}) \tag{45}$$

Where the superscript l and r denotes the value just left of the cell interface and just right of the cell interface respectively. Since in general $F_{i-1}(U) \neq F_i(U)$ we have $U^l_{i-1/2} \neq U^r_{i-1/2}$. There is thus a spatial discontinuity of U at cell interfaces.
When we apply the chain rule to (44) we get

$$\begin{aligned} \frac{\partial U}{\partial t} + \frac{\partial F_{i-1}(U)}{\partial U}\frac{\partial U}{\partial x} = 0, \text{ if } x < x_{i-1/2} \\ \frac{\partial U}{\partial t} + \frac{\partial F_i(U)}{\partial U}\frac{\partial U}{\partial x} = 0, \text{ if } x > x_{i-1/2} \end{aligned} \tag{46}$$

Here $\frac{\partial F_i(U)}{\partial U} = H_i(U)$ is the flux Jacobian as introduced in (25).
The next simplification is the assumption that the flux Jacobian is constant in each cell $H_i(U) = H^n_i$ in cell C_i at t^n. Thus we arrive at a system of two linear PDEs for the Riemann problem.
This 2 x 2 linear system of strictly hyperbolic PDEs has two characteristic variables with corresponding constant eigenvectors and constant eigenvalues. As we have assumed that the problem is subcritical, there is one characteristic variable moving to the left and one to the right. We are interested what happens at the discontinuity as this will affect the value of U^{n+1}. At t^n we have piecewise continuous initial data, U^n_{i-1} and U^n_i. We thus expect the leftward flowing characteristic variable that starts at the cell interface to move at speed $\lambda^n_{2,i-1}$ into the C_{i-1} domain. Similarly the rightward flowing characteristic variable moves at $\lambda^n_{1,i}$ into the C_i domain. So at t^{n+1}, the U domain is piecewise constant with four values, namely U^n_{i-1}, $U^l_{i-1/2}$,$U^r_{i-1/2}$ and U^n_i. How much the values of U_{i-1} and U_i change over time, depends on the two added discontinuities. These discontinuities are the waves. We will investigate their behaviour more thoroughly.
The eigenvectors and eigenvalues of the flux Jacobian are given by

$$\lambda_1 = u + c, \quad r_1 = \begin{bmatrix} \frac{A}{2c} \\ \frac{1}{2} \end{bmatrix}, \quad \lambda_2 = u - c, \quad r_2 = \begin{bmatrix} -\frac{A}{2c} \\ \frac{1}{2} \end{bmatrix} \tag{47}$$

Using our insight from above as justification, we will use for the rightward flowing waves

$$\lambda^n_{1,i-1/2} = \lambda^n_{1,i}, \quad r^n_{1,i-1/2} = r^n_{1,i} \tag{48}$$

And for the leftward flowing wave we use

$$\lambda^n_{2,i-1/2} = \lambda^n_{2,i-1}, \quad r^n_{2,i-1/2} = r^n_{2,i-1} \tag{49}$$

We will now solve for the strength of these waves, and thus determine U^{n+1} by averaging the effects of the waves. To solve this problem, one could try to find $U^l_{i-1/2}$ and $U^r_{i-1/2}$. This, however, proves to be a difficult task. Focusing on the flux is the simpler approach. To this end, we will use the continuity of the flux at the cell interface and decompose the flux difference $F^n_i(U) - F^n_{i-1}(U)$ into f-waves, this is the flux difference splitting. To achieve this, we use that the first f-wave, $\mathcal{Z}^n_{1,i-1/2}$, is proportional to $r^n_{1,i}$ and the second f-wave, $\mathcal{Z}^n_{2,i-1/2}$, is proportional to $r^n_{2,i-1}$. Decomposing the flux difference is done as follows

$$\begin{aligned} F_i(U) - F_{i-1}(U) &= \mathcal{Z}^n_{1,i-1/2} + \mathcal{Z}^n_{2,i-1/2} = \beta^n_{1,i-1/2} r^n_{1,i} + \beta^n_{2,i-1/2} r^n_{2,i-1} \\ &= R^n_{i-1/2}\beta^n_{i-1/2} = \frac{1}{2}\begin{bmatrix} \frac{A^n_i}{c^n_i} & -\frac{A^n_{i-1}}{c^n_{i-1}} \\ 1 & 1 \end{bmatrix}\begin{bmatrix} \beta^n_{1,i-1/2} \\ \beta^n_{2,i-1/2} \end{bmatrix} \end{aligned} \tag{50}$$

Here the factor $\beta^n_{j,i-1/2}$ is the relative strength of the eigenvector $r^n_{j,i-1/2}$. $R^n_{i-1/2}$ contains both eigenvectors as columns. Solving for $\beta^n_{i-1/2}$

$$\begin{bmatrix} \beta^n_{1,i-1/2} \\ \beta^n_{2,i-1/2} \end{bmatrix} = \frac{2}{\frac{A^n_i}{c^n_i} + \frac{A^n_{i-1}}{c^n_{i-1}}}\begin{bmatrix} 1 & \frac{A^n_{i-1}}{c^n_{i-1}} \\ -1 & \frac{A^n_i}{c_i} \end{bmatrix}\left(F_i(U) - F_{i-1}(U)\right) \tag{51}$$

We can now calculate the f-waves via $\mathcal{Z}^n_{j,i-1/2} = \beta^n_{j,i-1/2} r^n_{j,i-1/2}$.
The f-waves we have calculated are the effect of all waves flowing through the boundary, it thus comes as no surprise that we can incorporate them in the formalism introduced in the linear test case solution via

$$\begin{aligned} A^+ \Delta U^n_{i-1/2} &= \mathcal{Z}^n_{1,i-1/2} \\ A^- \Delta U^n_{i-1/2} &= \mathcal{Z}^n_{2,i-1/2} \end{aligned} \tag{52}$$

Now we can formulate the method for the nonlinear case, it is given by

$$U^{n+1}_i = U^n_i - \frac{\Delta t}{\Delta x}\left(\mathcal{Z}^n_{1,i-1/2} + \mathcal{Z}^n_{2,i+1/2}\right) \tag{53}$$

5.4 High Resolution method

Flux differencing methods as the one described above have the undesirable trait that they smear out solutions and thus do not have a high resolution. To improve the solution found, we would like to increase the resolution. However, Godunov's order barrier theorem states linear methods higher than first order cannot provide non-oscillatory solutions. To increase the resolution, we are thus required to use a nonlinear method. We will use flux limiters. Flux limiters work by switching between different spatial discretization schemes. Solutions containing a steep gradient are solved using a first order scheme so as to not have oscillations. When the gradient is less steep, a higher order spatial discretization is used to improve resolution. It is not a hard on/off switching that takes place, but more like a spectrum that the flux limiter uses. The method is formulated as

$$U^{n+1}_i = U^n_i - \frac{\Delta t}{\Delta x}\left(\mathcal{Z}^n_{1,i-1/2} + \mathcal{Z}^n_{2,i+1/2}\right) - \frac{\Delta t}{\Delta x}\left(\tilde{\mathcal{F}}^n_{i+1/2} - \tilde{\mathcal{F}}^n_{i-1/2}\right) \tag{54}$$

Here $\tilde{\mathcal{F}}^n_{i-1/2}$ is a flux correction term given by

$$\tilde{\mathcal{F}}^n_{i-1/2} = \frac{1}{2}\sum_{p=1}^{2} \operatorname{sign}\left(\lambda^n_{p,i-1/2}\right)\left(1 - \frac{\Delta t}{\Delta x}\left|\lambda^n_{p,i-1/2}\right|\right)\tilde{\mathcal{Z}}^n_{p,i-1/2} \tag{55}$$

$\tilde{\mathcal{Z}}^n_{p,i-1/2}$ is a modified version of $\mathcal{Z}^n_{p,i-1/2}$

$$\tilde{\mathcal{Z}}^n_{p,i-1/2} = \phi\left(\theta^n_{p,i-1/2}\right)\mathcal{Z}^n_{p,i-1/2} \tag{56}$$

Where $\phi(\theta)$ is the flux limiter. In this case the minmod limiter is used, this is second order Total Variation Diminishing (TVD). This is a sufficient condition to guarantee stability

$$\phi_{mm}(\theta) = \max\left\{0, \min\left\{2\theta, \frac{2+\theta}{3}, 2\right\}\right\} \tag{57}$$

The argument of the flux limiter is a measure of the strength of the waves that will reach the cell in the next time step relative to $\mathcal{Z}^n_{p,i-1/2}$. This depends on the propagating directions of the waves, given by $\lambda^n_{p,i-1/2}$. In [13], a method is proposed to determine the wave strength.

$$\theta^n_{p,i-1/2} = \frac{\mathcal{Z}^n_{p,I-1/2} \cdot \mathcal{Z}^n_{p,i-1/2}}{\mathcal{Z}^n_{p,i-1/2} \cdot \mathcal{Z}^n_{p,i-1/2}} \tag{58}$$

Here the dot represents the dot product between vectors. I is given by

$$I = \begin{cases} i-1 & \text{if } \lambda^n_{p,i-1/2} > 0 \\ i+1 & \text{if } \lambda^n_{p,i-1/2} < 0 \end{cases} \tag{59}$$

This method only works if the solution is smooth enough. If the solution changes extremely rapidly, more sophisticated methods are needed, an example is presented in Lax and Liu [6].

5.5 Frictional forces

If we assume the frictional forces to be non-negligible, we have to include them in our numerical method. This will be the case in the 111-artery model. In this case $\mu = 0.035\ P$ for blood and the frictional force is included via a first order discretization, giving a third term. Then the method is given by

$$U_i^{n+1} = U_i^n - \frac{\Delta t}{\Delta x}\left(\mathcal{Z}^n_{1,i-1/2} + \mathcal{Z}^n_{2,i+1/2}\right) - \frac{\Delta t}{\Delta x}\left(\tilde{\mathcal{F}}^n_{i+1/2} - \tilde{\mathcal{F}}^n_{i-1/2}\right) + \Delta t\ S_i^n(U) \tag{60}$$

With $S_i^n(U)$ given by

$$S_i^n(U) = \begin{bmatrix} 0 \\ -8\pi\mu \frac{u_i^n}{A_i^n \rho} \end{bmatrix} \tag{61}$$

5.6 Boundary conditions

We perform an analysis to determine which variables we can describe at the boundaries. Here the characteristic variables are useful, since the variables at a given point in the system are a combination of forward and backward travelling waves. At the boundary we thus only need to prescribe the incoming wave front from outside the computational domain. Since the characteristic variable w_1 corresponds to $\lambda_1 > 0$ and w_2 corresponds to $\lambda_2 < 0$, we need to prescribe w_1 at the left boundary and w_2 at the right boundary. To determine which variable we can describe, we compute

$$J_{w_1} = \frac{\partial(A,u)}{\partial w_1} = \begin{bmatrix} \left(\frac{\rho}{2\beta}\right)^2 \left(\frac{w_1 - w_2}{4}\right)^3 \\ \frac{1}{2} \end{bmatrix} \tag{62}$$

And

$$J_{w_2} = \frac{\partial(A,u)}{\partial w_2} = \begin{bmatrix} -\left(\frac{\rho}{2\beta}\right)^2 \left(\frac{w_1 - w_2}{4}\right)^3 \\ \frac{1}{2} \end{bmatrix} \tag{63}$$

We can use a variable to prescribe a characteristic if the corresponding element of J_{w_j} is nonzero. For u this is obviously the case. We can prescribe A whenever $w_1 \neq w_2$. This is the case when $-4c \neq 4c \Rightarrow c \neq -c \Rightarrow c \neq 0$. Since under normal physiological circumstances $\beta > 0, \rho > 0, A > 0$ it follows from $c = \sqrt{\frac{\beta}{2\rho}} A^{1/4}$ that indeed $c > 0$. We can thus prescribe A or u or any function of the two such as p or Q.

5.7 Forward prescription

When dealing with boundary conditions, one usually chooses to prescribe a certain variable such that a specific condition is met at the boundary. However, if one would bluntly prescribe p, A, u or Q, at the inlet boundary, you would need to have knowledge of the backward running waves. Stents, bifurcations and their location in the system affect these waves among other things. Lacking this knowledge, it would be more natural to prescribe variables using the forward propagating characteristic w_1 and fixing w_2 in its initial state. The forward prescription ensures that the boundary conditions are not sensitive to the backward running waves. It is important to note that when $forward$ prescription is used, the value at the boundary is not exactly equal to the given value. However, the difference between actual prescribed value and the $forward$ prescription is at most a few per cent, while having good non-reflective properties.

It is important to note that in the section Partially Patient-Specific Model, we will be dealing with absolute, not forward, flow rates.

In Appendix D, a test case with a stented artery is presented that provides insights into the basic workings of the model.

6 Modelling the circulation

In the preceding section, we have constructed a method of simulating pulse propagation through a single artery with possible discontinuous material properties. To properly model flow through the human arterial network, we need to have a way to model the heart (inflow boundary conditions), outflow boundary conditions and branching points. Various methods are used for the 55-artery network and the 111-artery network and we will explain the methods used.

6.1 Heart model

The heart is the driving factor of blood flow and is thus an extremely important part of every model. Two methods are used, a simple sinusoidal increase in cross-sectional area, and a more complicated model including the opening and closing of the aortic valve.

6.1.1 Sinusoidal model

The heart causes an increase in pressure at the beginning of the Ascending Aorta and in this way drives flow throughout the arterial network. Via equation (14) an increase in pressure is related to an increase in cross-sectional area. Thus the heart can be modelled as an increase of the area at the beginning of the Ascending Aorta. This method is used in the 55-artery model. The equation describing the cross-sectional area at the start of the Ascending Aorta as a function of time is given by

$$\bar{A}(t) = A_{0,1} + 1.587 \cdot \delta(t)\mathrm{H}(\delta(t)), \quad \delta(t) = \sin(\omega t + 0.628) - 0.588 \tag{64}$$

The model is plotted in Figure 3.

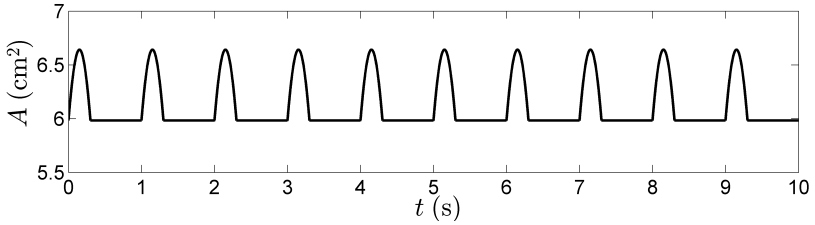

Figure 3: The heart model used for the 55-artery network using equation (64).

This model is easy to implement and does a good job of capturing the very basic properties of a heart.

6.1.2 Ventricular Pressure and Aortic Valve model

We will be using the model proposed by [4]. A schematic overview of this model is given in Figure 4.

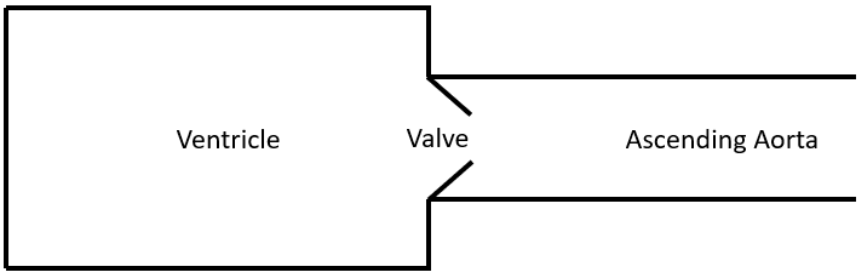

Figure 4: A schematic overview of the Ventricular Pressure and Aortic Valve model.

The heart is modelled by two components. First a predetermined cycle of ventricular (forward) pressure resembling the cycle of contraction and relaxation of the heart is considered. Second, a transmission/reflection function that resembles the aortic valve is used. The opening and closing of this valve is determined by local pressure and flow, as it would be in the human body. During systole, the phase where pressure increases in the aorta, the valve is open and the ventricular pressure pressure drives aortic flow. During diastole, when the pressure is decreasing in the aorta, the valve is closed and the aorta and ventricle are isolated.

The valve function is given by

$$V(t) = \frac{\left(e^{-kt} - 1\right)}{e^{-k} - 1} \tag{65}$$

Where $k = 3$. For $0 < t < 1$ this function increases from 0 to 1. This function is transformed to simulate the opening and closing of the valve. The motion of the valve is assumed to change rapidly at first and more slowly when it reaches its new position. The valve opens when the difference between ventricular and aortic pressure crosses 0 Pa. When the velocity of blood in the Ascending Aorta falls below -0.01 cm/s the valve starts to close rapidly. The Rapid Valve Opening Time (RVOT) is set 57 ms, the Rapid Valve Closing Time (RVCT) is set to 40 ms, both determined by Leyh et al. [14]. The opening and closing of the valve as modelled by V is illustrated in Figure 5.
The reflection coefficient, R, is defined as the fraction of backwards running waves that get reflected when they reach the aortic valve. It is defined as

$$R = -\frac{\Delta w_1}{\Delta w_2} = -\frac{w_1^{\mathrm{n+1}} - w_1^0}{w_2^{\mathrm{n+1}} - w_1^0} \tag{66}$$

Here w_2^{n+1} can be approximated by

$$w_2^{n+1}\big|_{x=x_0} = w_2^n\big|_{x=x_0-\lambda_2^n \Delta t} \tag{67}$$

The transmission coefficient, T, is defined as the fraction of forward running waves that get transmitted through the valve.
We relate the reflection and the transmission coefficient to V via

$$T = V, R = 1 - V \tag{68}$$

The heart cycle in the ventricle is described by four phases. First, *the isovolumic contraction*, the heart is contracting and pressure is building but the aortic valve is closed. Second, the *ejection phase*, the ventricular pressure rises above the aortic pressure and the valve opens. Blood flows from the ventricle through the aorta. The ventricle pressure is now driving aortic pressure. Thirdly, the *isovolumic relaxation phase*, the heart muscle relaxes causing a drop in pressure and flow. The aortic flow drops until it reaches zero when the valve closes. In this phase there is a small amount of reverse flow before the valve closes fully. Lastly, the *diastolic filling*, the heart relaxes and the ventricle increases in volume. This prepares the heart for another full cycle.

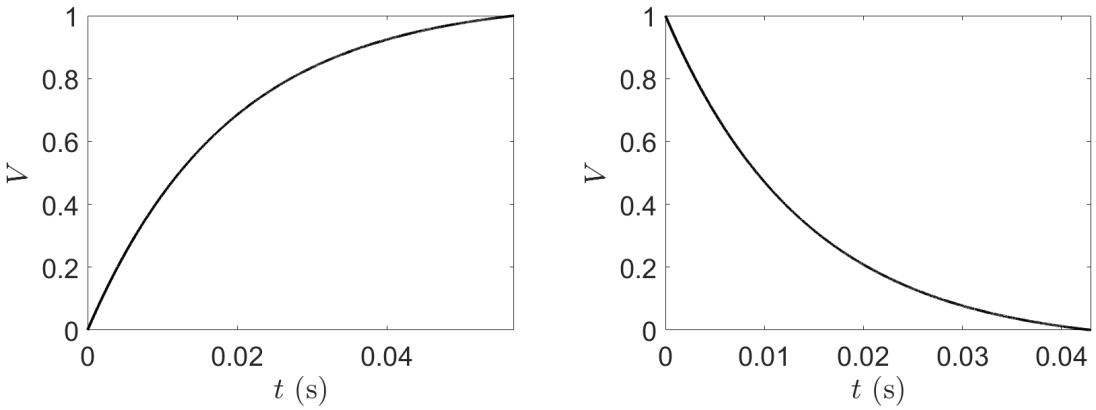

Figure 5: Left, opening of the valve and right closing of the valve.

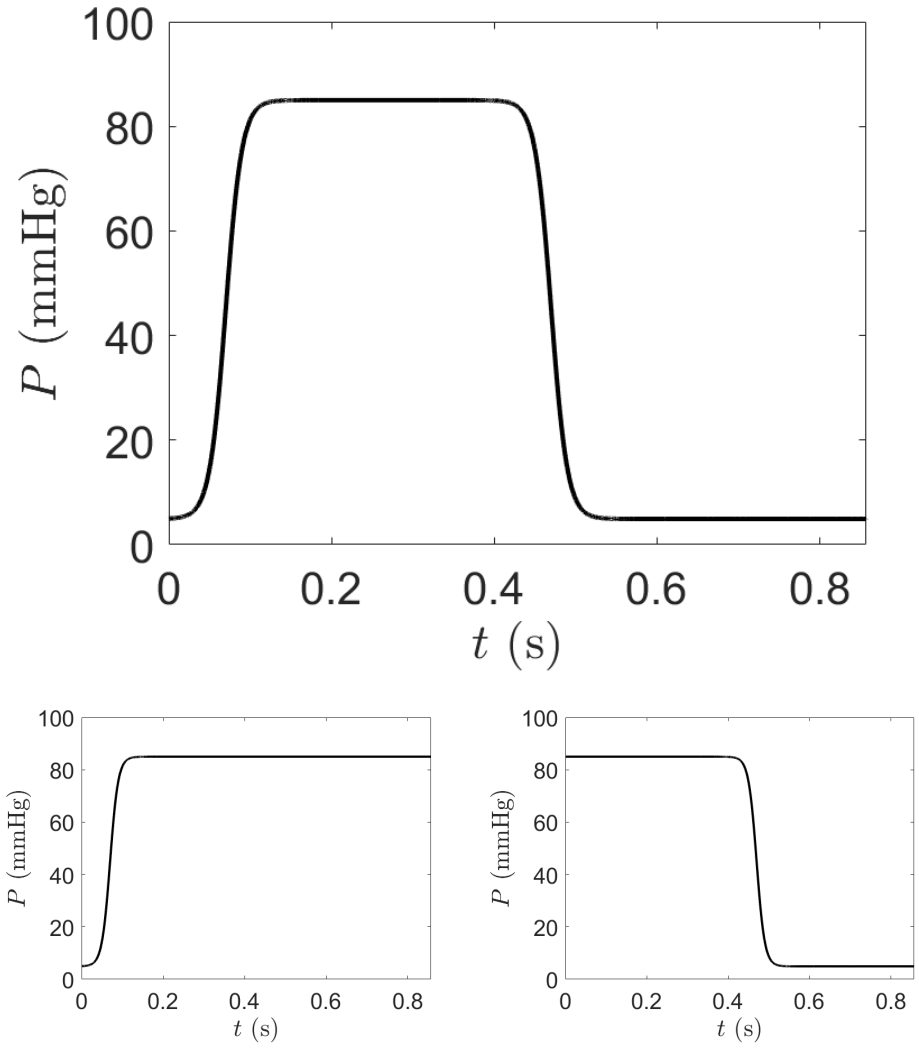

Figure 6: Top, the prescribed ventricular pressure used in the 111-artery network. Bottom, the two sigmoids used to create the prescribed pressure function. Pressure is given in mmHg.

The ventricular pressure is represented by a combination of two sigmoid functions. They have the form of

$$p_{\mathrm{sig}}(t) = a_1 + \frac{(a_2 - a_1)}{1 + e^{(a_3 - t)/a_4}} \tag{69}$$

with the coefficients given by

$$\begin{aligned} a_1 &= p_{\mathrm{ed}} - 9.11 \times 10^{-4} p_{\mathrm{peak}} \\ a_2 &= p_{\mathrm{peak}} \\ a_3 &= 7 t_{\mathrm{c}} \\ a_4 &= t_{\mathrm{c}} \end{aligned} \tag{70}$$

Where, p_{peak} is the peak pressure and p_{ed} is the end diastolic pressure. t_{c} is a time constant that determines the slope of the *isovolumic contraction* and the *isovolumic relaxation*. One whole cycle is described by one sigmoid describing the contraction phase and another, translated, sigmoid, describing the relaxation. In the 111-artery model we will be using two sigmoids with the same t_{c}, in this case fusing the sigmoids can be achieved by calculating where they intersect at peak pressure and switching at this point. Copying one cycle in time results in a heartbeat. A discontinuity at the end of the diastolic filling phase will not affect the system as the valve is already closed at that point. We set $t_c = 0.01$ s and shift the second sigmoid 0.54 to the left.

The two sigmoids are presented in the bottom row of Figure 6. The pressure is given in mmHg, the standard unit for pressure in medical fields. $1\ \mathrm{mmHg} \approx 133.322\ \mathrm{Pa}$.

To achieve flow, the heart must overcome aortic pressure. If aortic pressure increases the ventricle increases its pressure accordingly to sustain flow. This phenomenon is known as afterload $p_{LV^a}(t)$. This afterload pressure is caused by backwards running waves. Combining equations (14) and (30) we can calculate the pressure change due to a change in w_2, it is weighted by R to yield

$$p_{LV^a}(t) = (1-R)\,\frac{\rho}{32}\left[w_2(t)^2 - \left(w_2^0\right)^2 + 2w_1(t)\left(w_2^0 - w_2(t)\right)\right] \tag{71}$$

The total pressure in the ventricle is then

$$p_{LV}(t) = \bar{p}_{LV}(t) + p_{LV^a}(t) \tag{72}$$

Where $\bar{p}_{LV}(t)$ denotes the prescribe pressure.

The total value of $w_{1,\mathrm{in}}$ is given by

$$w_{1,\mathrm{in}} = \Delta w_{1\mathrm{p}} + \Delta w_{1\mathrm{r}} + w_1^0 \tag{73}$$

Where w_1^0 is the initial value, $\Delta w_{1\mathrm{p}}$ is the change in the incoming characteristic variable caused by the pressure difference between ventricle and aorta. $\Delta w_{1\mathrm{r}}$ is the change in characteristic associated with the backwards running wave being reflected by the valve. $\Delta w_{1\mathrm{p}}$ is given by

$$\Delta w_{1\mathrm{p}} = T\Delta w_1 \tag{74}$$

Where Δw_1 denotes the change in the characteristic due to the pressure difference, which is then weighed with T. Furthermore, $\Delta w_{1\mathrm{r}}$ is given by

$$\Delta w_{1\mathrm{r}} = -R\Delta w_2 \tag{75}$$

Where Δw_2 is the change in the backward running characteristic which is weighed by R to simulate waves being reflected.

This comprises the whole Ventricular Pressure and Aortic Valve model. It will be used for the 111-artery model with parameters $p_{\mathrm{ed}} = 5\ \mathrm{mmHg}$, $p_{\mathrm{peak}} = 85\ \mathrm{mmHg}$, $t_c = 0.01\ \mathrm{ms}$ and a heart rate of 70 beats/min.

6.2 Outlet boundary conditions

In principle, the human arterial tree is a circular system. It consists, however, out of immensely many small arteries that are impossible to measure individually. The number of branches increases dramatically at the terminal end of the network and consists of millions of capillaries. Thus when modelling the arterial network it must be truncated at a certain point. There have been many different approaches. Researches have developed close loop models that have the benefit of being physiologically more realistic Mynard and Smolich [10]. They use a model for a vascular bed that is filled and drained by respectively arteries and veins.
Models that exclude the veins and thus the circular nature of the arterial network can still produce realistic results. These models truncate after a few generations of branching. A creative way to treat terminal vessels has been using tapering arteries as terminal elements [4]. The methods that we will use are a terminal reflection coefficient and the three-element windkessel model.

6.2.1 Terminal reflection coefficient

As waves propagate through the arterial network, they will partially be reflected the further they travel. A simple model assumes these effects are only resistive and approximates their combined effect at the terminal vessels of the network. It is possible then to define the reflection coefficient as

$$R_t = -\frac{\Delta w_2}{\Delta w_1} = -\frac{w_2^{n+1} - w_2^0}{w_1^{n+1} - w_1^0} \tag{76}$$

Here w_1^{n+1} can be approximated by

$$w_1^{n+1}\big|_{x=x_L} = w_1^n|_{x=x_L-\lambda_1^n \Delta t} \tag{77}$$

Here $x = x_L$ denotes the end of a vessel. w_1^0 and w_2^0 are the initial values of the characteristics. Solving for w_2^{n+1} gives

$$w_2^{n+1} = w_2^0 - R_t \left(w_1^{n+1} - w_1^0\right) \tag{78}$$

A reflection coefficient of 1 corresponds to 100% reflection whilst a coefficient of 0 corresponds to a free outflow condition. We have of course $R_t \in [0, 1]$. The value of R_t needs to be documented for every terminal vessel. This approach is reasonably accurate but does not take into account the known capacitive properties of a vascular bed. It will be used in the 55-artery network.

6.2.2 Windkessel model

The windkessel model has a rich history in simulating blood flow. It is an electrical circuit analogy to blood flow where Pressure (P) takes the role of Voltage (V), and flow (Q) takes on the role of current (I). The first analysis of a windkessel model was performed by Frank [11]. This concerned a two-element windkessel element consisting of a capacitor in parallel to a resistor. The resistor models the resistive properties in blood vessel whilst the capacitor accounts for compliance. Since then multiple variations have been composed, the most popular being the three-element version. There is however also a four-element windkessel that includes an inductor to account for fluid inertia.

With the rise of computation power the windkessel model ceased to be used for simulations of sizeable parts of the network. The three-element version is used extensively as a boundary condition as it does account for the compliance of blood vessels.
In Figure 7 it is shown how a windkessel element is coupled to a 1D network. C_{vb} and R_{vb} need to be determined experimentally, Z is the characteristic impedance of the 1D blood vessel and is given by

$$Z_{\text{1D}} = \frac{\rho c_{\text{1D}}}{A_{\text{1D}}} \tag{79}$$

In general, a windkessel element is governed by the following PDE which can be easily retrieved using standard voltage and current division rules

$$\left(1 + \frac{R_1}{R_2}\right) q + C R_1 \frac{dq}{dt} = C \frac{dp}{dt} + \frac{p - P^\infty}{R_2} \tag{80}$$

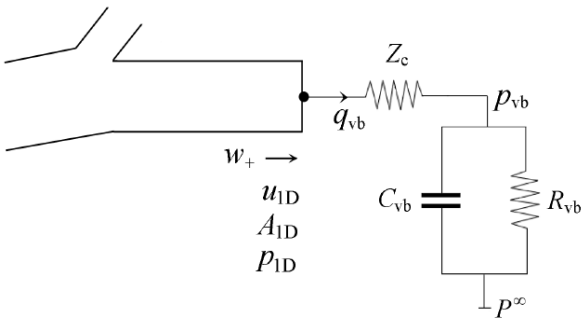

Figure 7: A three-element windkessel modelled coupled to a terminal vessel, from Mynard [5].

To determine the boundary conditions the following procedure is used. First continuity of flow is assumed, $q_{\mathrm{vb}} = q_{\mathrm{1D}} = A_{\mathrm{1D}} u_{\mathrm{1D}}$. Then, using the equation for flow in the three-element windkessel

$$q_{\mathrm{vb}} = C_{\mathrm{vb}} \frac{dp_{\mathrm{vb}}}{dt} + \frac{p_{\mathrm{vb}} - P^{\infty}}{R_{\mathrm{vb}}} \tag{81}$$

Using a first order discretisation gives an expressing for p_{vb}^{n+1}

$$p_{\mathrm{vb}}^{n+1} = p_{\mathrm{vb}}^{n} + \frac{\Delta t}{C_{\mathrm{vb}}} \left(A_{\mathrm{1D}} u_{\mathrm{1D}} - \frac{p_{\mathrm{vb}}^{n} - P^{\infty}}{R_{\mathrm{vb}}} \right) \tag{82}$$

The vascular bed flow can be found via

$$q_{\mathrm{vb}}^{n+1} = A_{\mathrm{1D}}^{n+1} u_{\mathrm{1D}}^{n+1} = \frac{p_{\mathrm{1D}}^{n+1} - p_{\mathrm{vb}}^{n+1}}{Z_{\mathrm{1D}}} \tag{83}$$

Now using $w_{1,\mathrm{1D}}^{n+1}$ we can write this as

$$A_{\mathrm{1D}}^{n+1} \left[w_{1,\mathrm{1D}}^{n+1} - 4 {A_{\mathrm{1D}}^{n+1}}^{1/4} \sqrt{\frac{\beta}{2\rho}} \right] = \frac{p_{\mathrm{1D}}^{n+1} - p_{\mathrm{vb}}^{n+1}}{Z_{\mathrm{1D}}} \tag{84}$$

Which, using equation (14) is a nonlinear expression for A_{1D}^{n+1} and is solved using the Newton-Raphson method. Afterwards, u_{1D}^{n+1} can be retrieved using $w_{1,\mathrm{1D}}^{n+1}$.

The three-element windkessel boundary condition model is used in the 111-artery network.

6.3 Branching points

A characteristic feature of the human arterial tree is the many branching points where one or multiple parent vessels connect to one or multiple daughter vessels. The most common branching point is a bifurcation where one parent vessel flows into two daughter vessels. Physically, any other combination of number of parent and daughter vessels is possible. The treatment of branching points is integral to having a realistic model outcome.

In Rozendaal [7] it was tried to combine the first element of both daughter vessels into one element and afterwards performing a splitting of the flux. The results were not unreasonable whilst dealing with a single bifurcation but the method had problems with simulating large networks of arteries. We will thus try a different approach.

We will treat branching points analogously to boundary conditions. More specifically, at the branching points we will force continuation of the characteristic variables as well as mass and pressure. The values obtained in this process will then be used to set boundary conditions for the parent and daughter vessels.

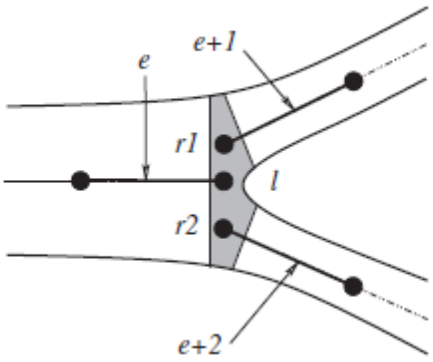

Figure 8: An illustration of a bifurcation with adjacent cells from Sherwin et al. [15].

If we look at Figure 8 we see a bifurcation along with its neighboring parent and daughter cells. With help of the continuation requirements, the boundary conditions are set in the gray area to both the parent and daughter vessel. In this case we have 6 variables we need to determine, namely the A and u couple for each vessel. We thus need 6 equations to solve the system. If we generalize this to I parent and J daughter vessels, we need $2(I+J)$ equations. The first half is determined by the outgoing characteristics, for the parent vessels we have

$$w_{1pi} = u_i + 4A_i^{1/4}\sqrt{\frac{\beta_i}{2\rho}} \tag{85}$$

Where w_{1pi} is determined at the cell bordering the branching point. For the daughter vessel we have

$$w_{2dj} = u_j - 4A_j^{1/4}\sqrt{\frac{\beta_j}{2\rho}} \tag{86}$$

Here w_{2dj} is determined analogously to w_{1pi}. The following equations are determined by forcing continuity of mass and pressure. Conservation of mass requires

$$Q = \sum_{i=1}^{I} A_i u_i = \sum_{j=1}^{J} A_j u_j \tag{87}$$

The remaining equations are provided by continuity of momentum, which for every parent-daughter pair reads

$$\frac{\rho u_i^2}{2} + p_{\text{ext}} + \beta_i(\sqrt{A_i} - \sqrt{A_{i0}}) = \frac{\rho u_j^2}{2} + p_{\text{ext}} + \beta_j(\sqrt{A_j} - \sqrt{A_{j0}}) \tag{88}$$

The equations can be written in the following way

$$\begin{aligned} f_1 &= u_p + 4A_p^{1/4}\sqrt{\tfrac{\beta_p}{2\rho}} - w_{1p} = 0 \\ f_{I+1} &= u_i - 4A_i^{1/4}\sqrt{\tfrac{\beta_i}{2\rho}} - w_{2i} = 0 \\ f_{I+J+1} &= \textstyle\sum_{i=1}^{I} u_i A_i - \sum_{j=1}^{J} u_j A_j = 0 \\ f_{2(I+J)} &= \tfrac{\rho}{2}u_I^2 + \beta_I(\sqrt{A_I} - \sqrt{A_{0I}}) - \tfrac{\rho}{2}u_J^2 - \beta_J(\sqrt{A_J} - \sqrt{A_{0J}}) = 0 \end{aligned} \tag{89}$$

We now define $\mathbf{f} = \begin{bmatrix} f_1 & \cdots & f_{2(I+J)} \end{bmatrix}^{\mathrm{T}}$. The Jacobian is given by

$$\mathbf{J} = \begin{bmatrix} \frac{\partial f_1}{\partial u_{i=1}} & \frac{\partial f_1}{\partial u_{i=2}} & \cdots & \frac{\partial f_1}{\partial u_{j=J}} & \frac{\partial f_1}{\partial A_{i=1}} & \frac{\partial f_1}{\partial A_{i=2}} & \cdots & \frac{\partial f_1}{\partial A_{j=J}} \\ \vdots & \vdots & \vdots & \vdots & \vdots & \vdots & \vdots & \vdots \\ \frac{\partial f_{2(I+J)}}{\partial u_{i=1}} & \frac{\partial f_{2(I+J)}}{\partial u_{i=2}} & \cdots & \frac{\partial f_{2(I+J)}}{\partial u_{j=J}} & \frac{\partial f_{2(I+J)}}{\partial A_{i=1}} & \frac{\partial f_{2(I+J)}}{\partial A_{i=2}} & \cdots & \frac{\partial f_{2(I+J)}}{\partial A_{j=J}} \end{bmatrix} \tag{90}$$

The system of equations can then be solved using the Newton-Raphson method for higher dimension which is given by

$$\mathbf{x}^{k+1} = \mathbf{x}^k - \left[\mathbf{J}^k\right]^{-1}\mathbf{f}^k \tag{91}$$

Where $\mathbf{x}$ contains the variables and k is the iteration number. As a stopping requirement the norm of $\mathbf{f}$ needs to fall below a certain value ϵ.

We will now present two test cases for the branching points. We will compare this method to the one used in [7]. To this end we will look at two kinds of bifurcations. It is important to state that our treatment of bifurcations is complemented by the formula for β given by equation (16). The inlet boundary condition is provided by

$$\bar{A}(t) = A_{0,p} + 0.1e^{-10^6(t-0.1)^2} \tag{92}$$

The outflow boundary condition is given by a free outflow condition ($R_t = 0$).

6.3.1 Test case - Bifurcation, constant total A_0

All test cases are performed in the Centimetre Gram Seconds (CGS) unit system as is costumary in literature. A conversion table can be found in Appendix A.

First we observe a bifurcation where $A_{0,\mathrm{P}} = 6\ \mathrm{cm}^2$ and $A_{0,\mathrm{D}_1} = A_{0,\mathrm{D}_2} = 3\ \mathrm{cm}^2$. Thus at the branching point the sum of the area of the daughter vessels is equal to that of the parent vessel. The values for β used in [7] are $\beta_{\mathrm{P}} = \beta_{\mathrm{D}_1} = \beta_{\mathrm{D}_2} = 10^5\ \mathrm{dyne/cm}^3$. Equation (16) results in $\beta_{\mathrm{P}} = 1.8345 \cdot 10^5\ \mathrm{dyne/cm}^3$ and $\beta_{\mathrm{D}_1} = \beta_{\mathrm{D}_2} = 2.5977 \cdot 10^5\ \mathrm{dyne/cm}^3$. The results are compared in Figure 9.

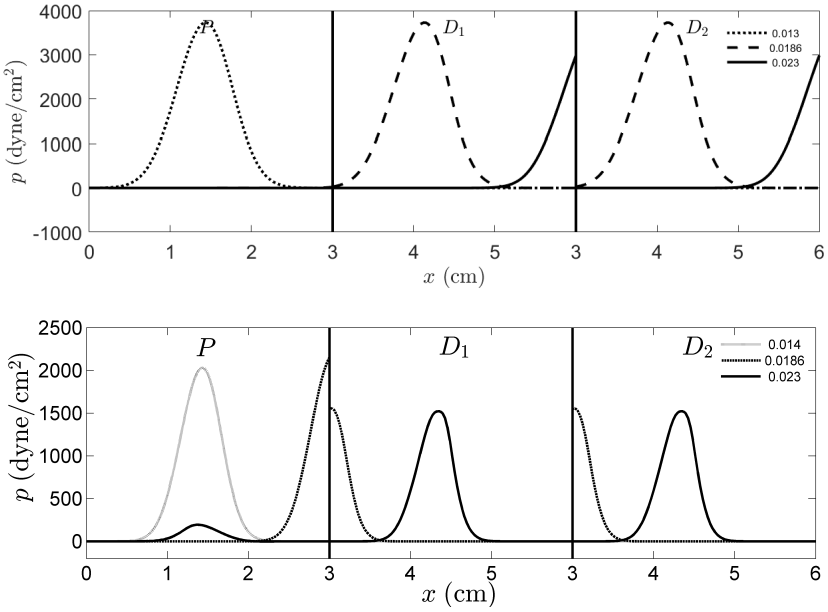

Figure 9: Results of wave propagation at a bifurcation with constant total A_0 shown for $t = 0.014$ s, $t = 0.0186$ s and at $t = 0.023$ s. The top row contains our model and the bottom row the one from [7].

Comparing the results from both models we see that the pressure in our model is higher, this is due to the higher values for β. Since the total cross-sectional area of the parent vessel and the sum of the daughter vessels are equal, we do not expect a reflected pressure wave of any kind. In the model of [7] there is such a wave present. In our model it is absent which points to a more realistic wave propagation at bifurcations.

6.3.2 Test case - Bifurcation, varying total A_0

Now we look at a bifurcation where $A_{0,\mathrm{P}} = 6\ \mathrm{cm}^2$, $A_{0,\mathrm{D}_1} = 6\ \mathrm{cm}^2$ and $A_{0,\mathrm{D}_2} = 3\ \mathrm{cm}^2$. Now the sum of the cross-sectional area of the daughter vessel is larger than that of the parent vessel. The values for β used in [7] are unchanged and given by $\beta_{\mathrm{P}} = \beta_{\mathrm{D}_1} = \beta_{\mathrm{D}_2} = 10^5\ \mathrm{dyne/cm}^3$. This time equation (16) results in $\beta_{\mathrm{P}} = 1.8345 \cdot 10^5\ \mathrm{dyne/cm}^3$, $\beta_{\mathrm{D}_1} = 1.8345 \cdot 10^5\ \mathrm{dyne/cm}^3$ and $\beta_{\mathrm{D}_2} = 2.5977 \cdot 10^5\ \mathrm{dyne/cm}^3$. The results are compared in Figure 10.

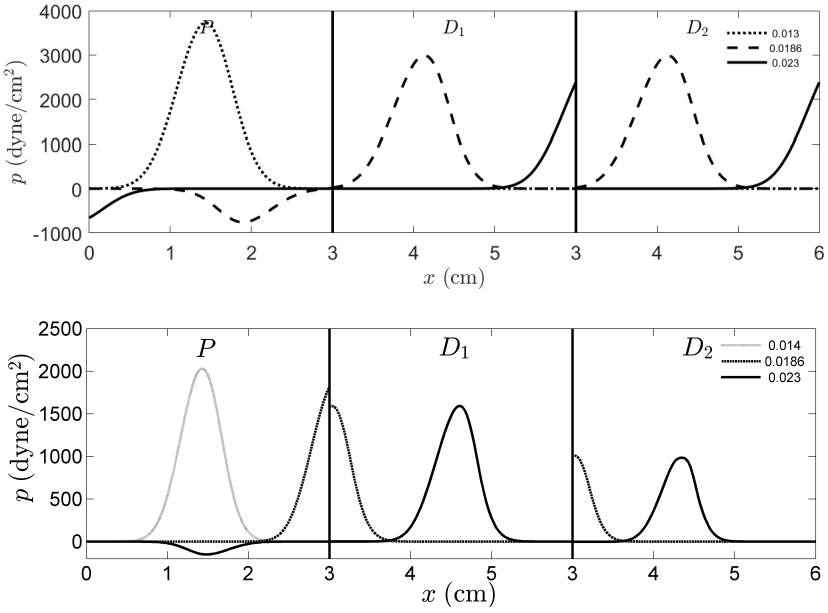

Figure 10: Results of wave propagation at a bifurcation with varying total A_0 shown for $t = 0.014$ s, $t = 0.0186$ s and at $t = 0.023$ s. The top row contains our model and the bottom row the one from [7].

Both models show a negative pressure wave propagating back into the parent vessel. That of our model is larger however. Another difference is the maximum of the pressure wave in both daughter vessels. Due to the method used in [7], the pressure in the smaller vessel is lower than that of the larger vessel. In our model this is not the case.

From these test cases it is evident that the models produce somewhat comparable result. It is not hard to see however that small difference at individual bifurcations can lead to big difference when dealing with a whole arterial network. All other branching points show similar behaviour and are not worth investigating on their own.

7 55-artery network

We have now discussed every aspect of our model. We will turn to the 55-artery model as a way of verifying the treatment of branching points in combination with the flux difference splitting method. Although it is not a verification with results obtained *in vivo* , which would be preferable, the Discontinuous Galerkin [4, 15] is a widely used method for 1D arterial network simulations and producing comparable results would be verification of the models capabilities. The connectivity of the network is given by a parent pointer matrix where a value of i at place j means that i is the parent vessel of vessel j. A 0 means that this vessel is adjacent to the inlet. It is given by Table 1 .

Table 1: Parent pointer of the 55-artery network. The top row represents the daughter vessels and the bottom row represents the parent vessels.

1	2	3	4	5	6	7	8	9	10	11	12	13	14	15	16	17	18	19	20	21	22	23	24	25	26	27	28
0	1	1	3	3	4	4	7	7	9	9	5	5	2	2	15	15	14	14	19	19	21	21	23	23	18	18	27
29	30	31	32	33	34	35	36	37	38	39	40	41	42	43	44	45	46	47	48	49	50	51	52	53	54	55	
27	29	29	30	30	28	28	35	35	37	37	39	39	41	41	42	42	44	44	46	46	43	43	50	50	52	52	

A visual representation of the arteries, their connectivity and place in the body is given in Figure 11. The physiological data is given in Table 6 and Table 7 in appendix B. The model is run for $T = 10$ s as to ensure a steady cycle is reached. The results are then represented for the last second of this 10 second period.

We will compare the results of our model, the model by Rozendaal [7] and the model by Sherwin et al. [15]. The results for the velocity, pressure wave forms and the characteristic variables are shown. In Figure 12 the results are shown at the start of the Ascending Aorta, artery 1. In Figure 13 the results are shown at the beginning of the L. Anterior Tibial, artery 49.

At the Ascending Aorta, we see the prescribed increase in A_0 in the shape of the w_1. Because we are prescribing forward variables, this is to be expected. Furthermore, the terminal reflection coefficients create backwards running wave of significant magnitude. As no bifurcation has yet been passed, the w_1 variables of all models behave the same. However, there is a notable difference in w_2, which has passed through bifurcations, between the model by [7] and the other two. The result is a complex velocity and pressure graph diverging significantly from prescribed values. The difference in results is then explained by the difference in w_2 which can be attributed to the bifurcation treatment.
At the l. anterior tibial we see that the forward running wave has increased dramatically in complexity. It has now passed several bifurcations which has resulted in different wave forms for [7] and the other two models. As the artery is a terminal artery we can see the behaviour of the terminal reflection coefficient well. It is clear that an increase in w_1 results in a scaled decrease of w_2 just as expected. Now the difference in results is primarily caused by w_1, which is then translated to w_2 by the terminal reflection coefficient. This again can be attributed to the bifurcation treatment.

The model from [7] produces the same overall shape as the one from [15]. It is clear from our analysis that the differences are caused by the bifurcation treatment. Changing the way bifurcations are treated has resulted in the flux difference splitting method producing highly comparable results to the Discontinuous Galerkin. The results from the 55-artery network provide a mathematical verification of our model. The quantities used (cross-sectional area and velocity of the blood) are not widely used in the medical field however. To investigate the models capability of producing medically applicable results we turn to the 111-artery network.

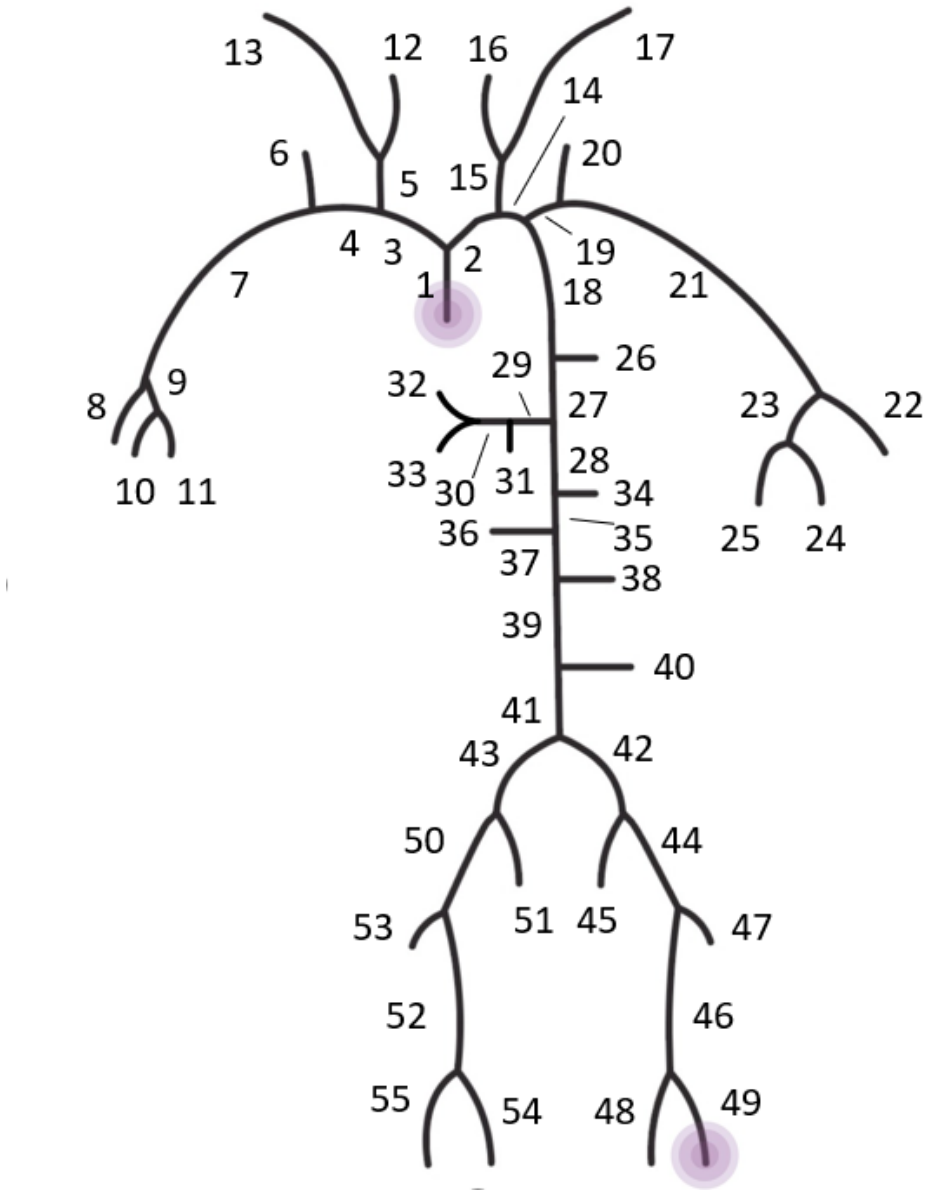

Figure 11: Connectivity of the 55 arteries and their location. The circles indicate where results are compared. Middle, Ascending Aorta and right the L. Anterior Tibial.

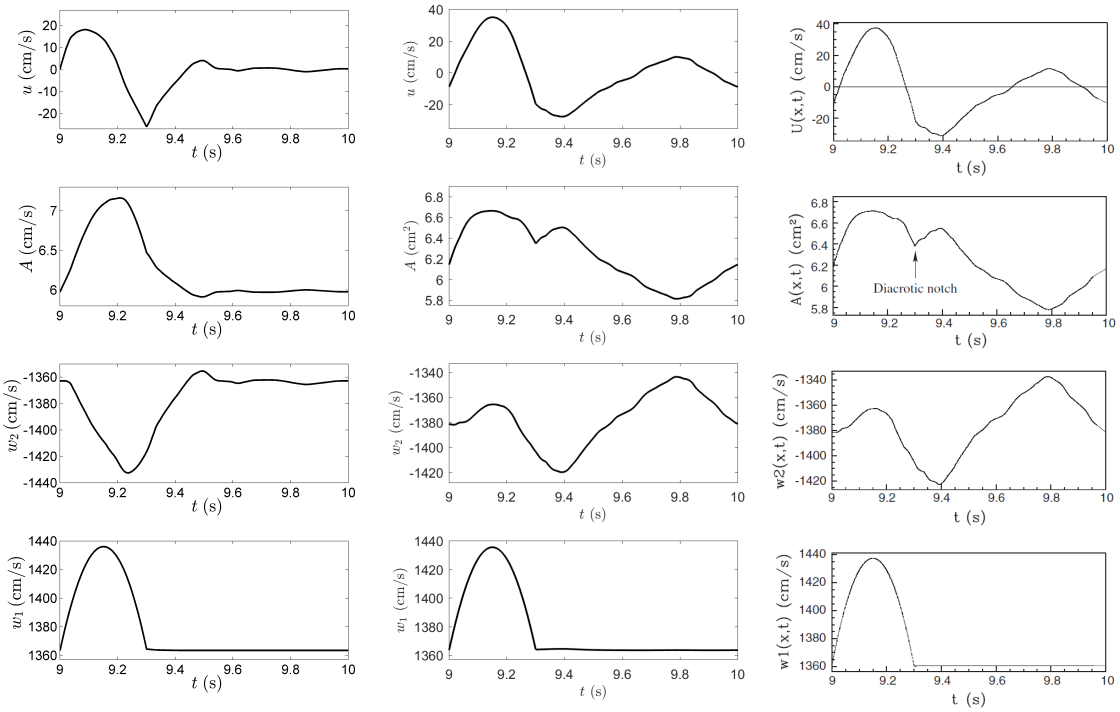

Figure 12: Results of the 55-artery network at the start of the Ascending Aorta. Left, the model from [7], middle, our model , right, the Discontinuous Galerkin, from [15].

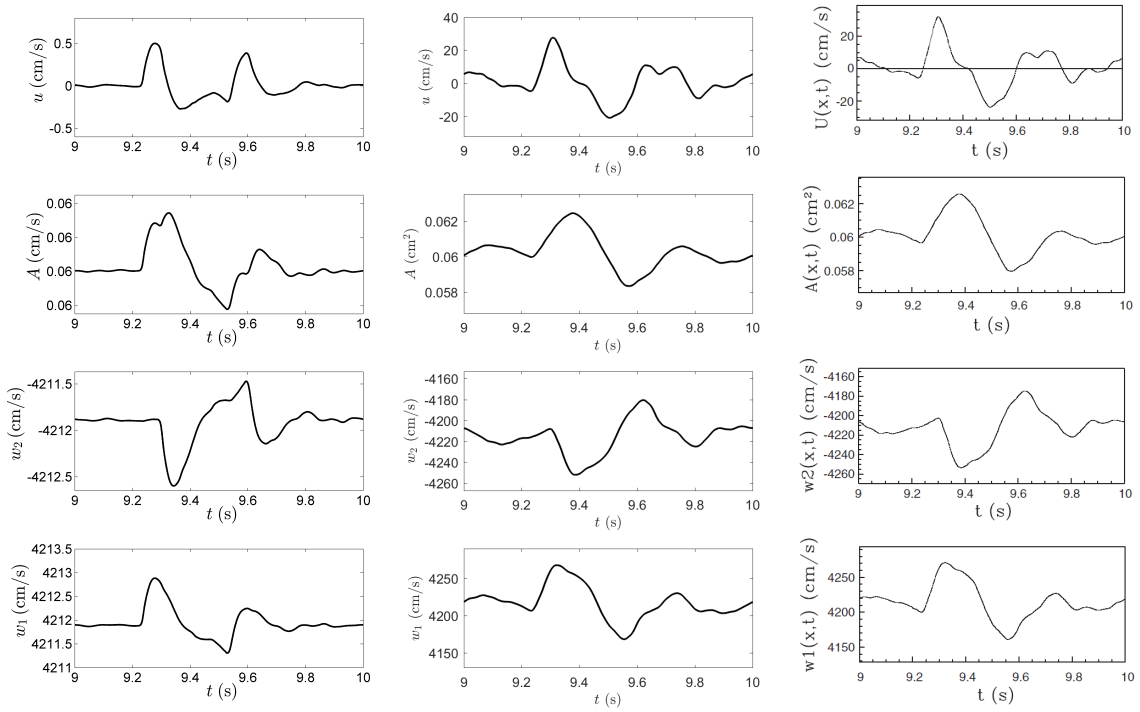

Figure 13: Results of the 55-artery network at the start of the L. Anterior Tibial. Left, the model from [7], middle, our model , right, the Discontinuous Galerkin, from [15].

8 111-artery network

We now turn our attention to the more detailed 111-artery network. The most notable difference is the addition of the circle of Willis of arteries in the brain and face/neck. The data from [10] forms the basis of this network. The study focuses on a circular model (including veins). The data is copied in the following way

- All non-coronary arteries were included with the exception of the the intercostal arteries.
- All terminal arteries were modelled as having their own windkessel boundary condition, as opposed to a collective vascular bed.
- Because of the exclusion of the intercostal arteries the Descending Thoracic Artery I & II were modelled as one single artery.

The coronary arteries and the intercostal arteries are relatively small and have a small mean flow. Their exclusion will not impact results in a meaningful way.
The data for the windkessel models is retrieved in the following way. If a terminal artery is present in the model and data from Stergiopulos et al. [16], the data is copied. If it is not, compliance values were taken directly from [10] and the vascular bed resistance is set to $R_{\mathrm{vb}} = R_{\mathrm{cap}} + Z_0$, where R_{cap} is the reference value reported by [10] and Z_0 is the characteristic impedance of the terminal vessel. This approach is warranted since [10] based his data on [16] and using $R_{\mathrm{vb}} = R_{\mathrm{cap}} + Z_0$ ensures the highest agreement between the vascular bed model and the windkessel model. For more information about vascular bed models, the reader is invited to [5].

The connectivity of the 111-artery network is shown in Figure 14. The circles indicate where in the network the results were compared. The physiological data for the 111-artery network is available in Appendix C.

For the 111-artery network we will change the variables we investigate to Q in $\mathrm{ml/s}$ and P (mmHg). This is done as these are the viable quantities and units in the medical field and thus it makes the results more understandable for medical experts. We will be comparing results to Mynard and Smolich [10]. Differences will be inevitable due to the vastly different approaches to network components and the differences between closed/open loop models. The variables for our artery network come from this study and thus it is still a viable comparison to investigate our model. They also provide *in vivo* results which are of extra interest. It is important to note that the *in vivo* results are taken from different sources and thus do not originate from the same person. Results from [10] are given in Figure 15.

The model is run for 10 periods to achieve a steady cycle. Results are shown in Figure 16.

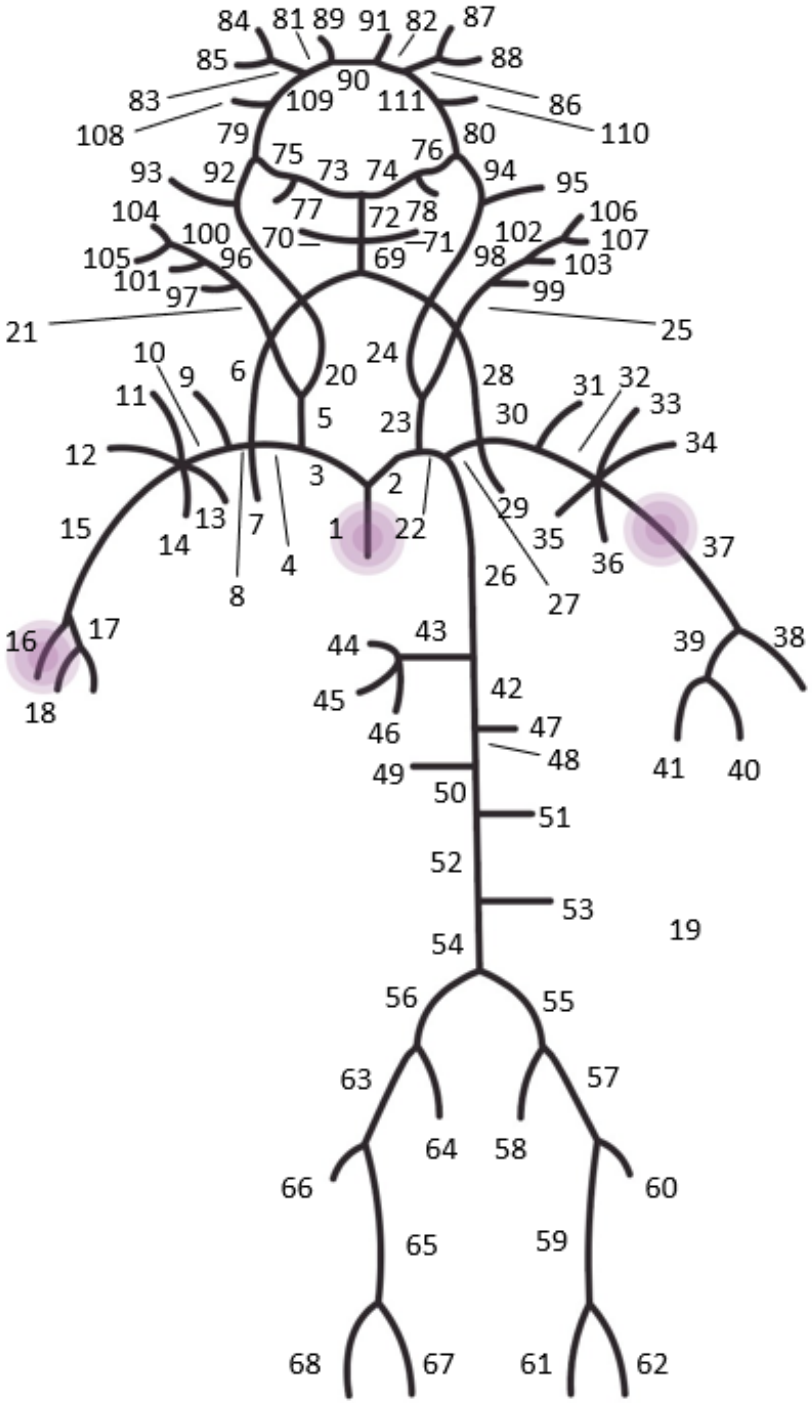

Figure 14: Connectivity of the 111 arteries. The circles indicate arteries where the results were compared, from left to right, Right Radial Artery, Ascending Aorta and the Left Brachial Artery.

8.1 Initial results

From Figure 16 it is immediately clear that the 111-artery network produces more complex results than the 55-artery network. Observing the incoming characteristic variable at the Ascending Aorta, we see the shape of the prescribed pressure returning in the systolic part of the cycle. First a rapid increase followed by a plateau.

When the ventricle pressure starts to drop, the valve plays an important role in shaping the pressure wave form. As soon as the flow becomes negative, the valve starts to close. Before it fully closes, there is a period of net negative flow, during this period the pressure drops. When the valve fully closes, flow returns to zero and this is accompanied by an increase in pressure. This phenomena is known as a dicrotic notch. After the dicrotic notch, the pressure gradually starts to come down.

Further down into the network, we see both at the Right Radial Artery and the Left Brachial Artery that the diastolic (minimum) pressure has dropped as a consequence of the frictional forces. At these terminal vessels we see that the windkessel element acts in about the same way as the reflection coefficient. Namely, an increase in w_1 is turned into a scaled decrease in w_2. In the windkessel case, we see a smoothing of the curve however. This is due to the windkessel element being frequency sensitive and reflecting lower frequency waves more.

We will now compare our results with that of the closed loop model and the *in vivo* measurements given in Figure 15. We will compare our results at the Ascending Aorta to results at the Aortic Root from [10]. There are only two small arteries that branch of the Aortic Root before it turns into the Ascending Aorta so a comparison is justified. At the Aortic Root/Ascending Aorta we see a comparable shape of the pressure wave of same magnitude. The differences can be best understood by observing the flow wave. We see that our model has a relatively fast increase to peak flow, resulting in a short fast increase of pressure at the beginning of systole. The gradual decrease after peak pressure takes a longer time, resulting in a longer slow increase in pressure to peak pressure. Lastly, there is more negative flow, resulting in a bigger dip in pressure right after peak pressure.

At the Right Radial Artery and the Left Brachial Artery the difference is more profound. The shape of the pressure wave at the Right Radial is somewhat comparable. However, peak pressure value is significantly lower and the second peak is relatively large.
At the Left Brachial we do not see a peak in pressure of any kind as the pressure plateaus at around $120\ \mathrm{mmHg}$. This behaviour is also seen in w_1. If we look at the Ascending Aorta we see this same plateau in w_1.

Both differences are likely to be attributed to the difference of boundary conditions at the Aortic Root/Ascending Aorta and are not caused by any big differences in the numerical methods used. If we wish to achieve more comparable results, we thus need to change our inflow boundary conditions. The difference in pressure at the Aortic Root/Ascending Aorta hints at a more slowly rising boundary condition during systole. The difference at the Left Brachial suggest prescribing ventricular pressure with a peak value instead of a plateau.

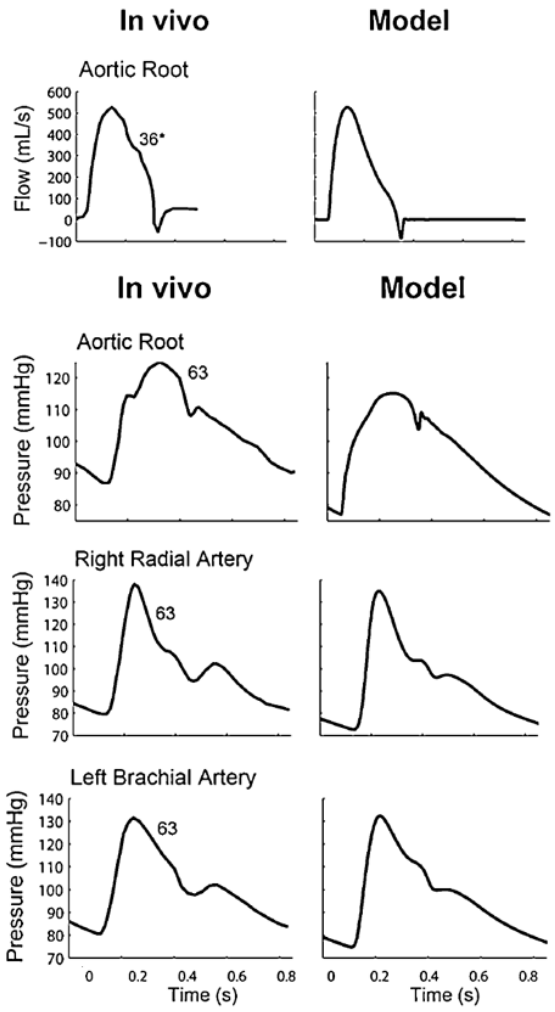

Figure 15: Results from the closed loop model and *in vivo* measurements, both from [10].

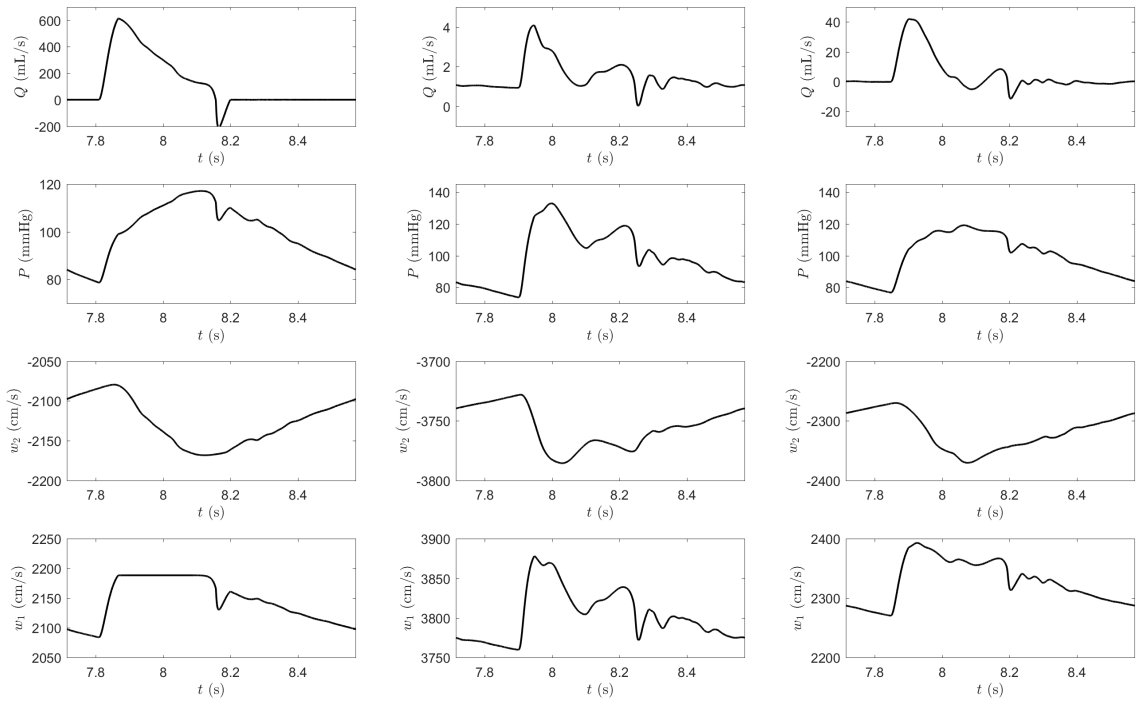

Figure 16: Results of the 111-artery network at the start of the Ascending Aorta, left, the Right Radial Artery, right, and the Left Brachial Artery, bottom. Results are shown for one period.

8.2 Adjusted ventricular pressure

Learning from the initial results, we strive to prescribe ventricular pressure to better match our results to that obtained *in vivo*. To this end we set $t_c = 0.055$ s, this will make the curve look more like a peak instead of a plateau. Because peak pressure is reached slower, we set $p_{\text{peak}} = 90$ mmHG so as to ensure mean pressure does not drop. We shifted the first curve 0.15 to the left and the second curve 1.1 to the left. The result is shown in Figure 17. There is a discontinuity at the start of a new period, this is of no concern however since the valve is closed at this point thus isolating the system from the prescribed ventricular pressure.

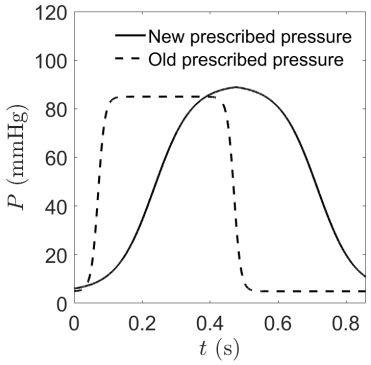

Figure 17: Newly prescribed pressure.

The results obtained by prescribing this ventricular pressure are shown in Figure 18. We have left out the characteristic variables as we have already analysed their behaviour.

The results obtained with the newly prescribed ventricular pressure bear a closer resemblance to *in vivo* results. At the Ascending Aorta the flow graph is more in line with results from [10], we also indeed see a more gradual increase of pressure at the Ascending Aorta. At the Right Radial the form and magnitude of the pressure wave closely resembles the *in vivo* results. At the Left Brachial there is also more of an appearance of a peak in pressure.

We can conclude that the newly prescribed pressure is a more realistic inflow boundary condition. Using the *in vivo* results we can again verify the models capability of producing realistic results.

Using the prescribed ventricular heart model combined with valve action and the windkessel model, we are capable of simulating realistic pressure and flow graphs. To ensure more realistic results, we could try to use more complicated models for the heart. This, however, often results in having to determine more values for more parameters. This not only increases uncertainty but also defeats the purpose of having a simple 1D model to begin with. If a model becomes ever more complex, it can not easily be used for patient-specific predictions.

To keep the simple nature of the model and be usable for patient-specific pressure predictions, we will transition from prescribed pressure, which is hard to measure inside an aorta, to prescribed flow, which can more easily be retrieved.

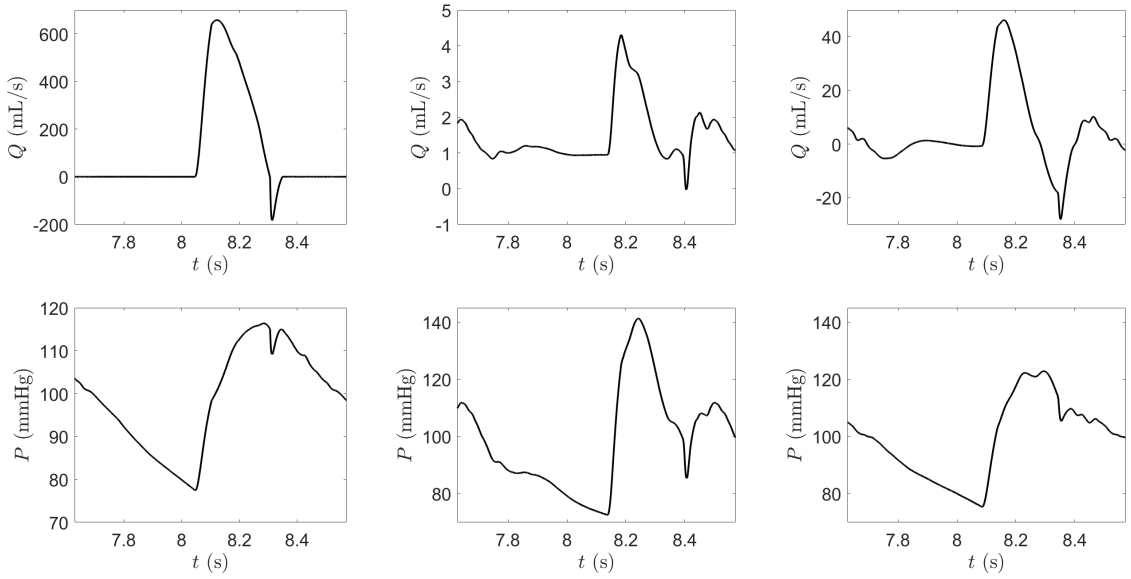

Figure 18: Results of the 111-artery network with the adjusted prescribed ventricular pressure at the start of the Ascending Aorta, left, the Right Radial Artery, middle, and the Left Brachial Artery, right. Results are shown for 1.1 period.

9 A partially patient-specific model

There are many potential applications of 1D blood flow model. One such application is noninvasive pressure measurement in the aorta. As an example, decisions to operate on an arterial condition known as aortic rupture are currently made by simply measuring the diameter with an MRI scan and comparing with a predetermined condition. If the aortic diameter is determined to be too large, it is decided to operate. This condition is not patient-specific however and it would be beneficiary to know the pressure cycle to determine if it is stable and safe.

It is possible however, with the same MRI scan, to determine the flow rate in the aorta. If the flow rate at the beginning of the Ascending Aorta is measured, a 1D model can in theory be used to determine pressure. Here a 1D model has a distinct advantage over a 3D model, namely that it produces absolute pressure values and not just a pressure gradient. Moreover, it has a far superior running time (circa 10 minutes versus a couple of days). In this section, we will attempt to produce such a partially patient-specific model using data acquired at the Leids Universitair Medisch Centrum (LUMC).

9.1 Method

We will describe the method we used to build the partially patient-specific model. There are two types of methods that were investigated. The single-factor scaling method and the multi-factor scaling method.

9.1.1 Inlet boundary conditions

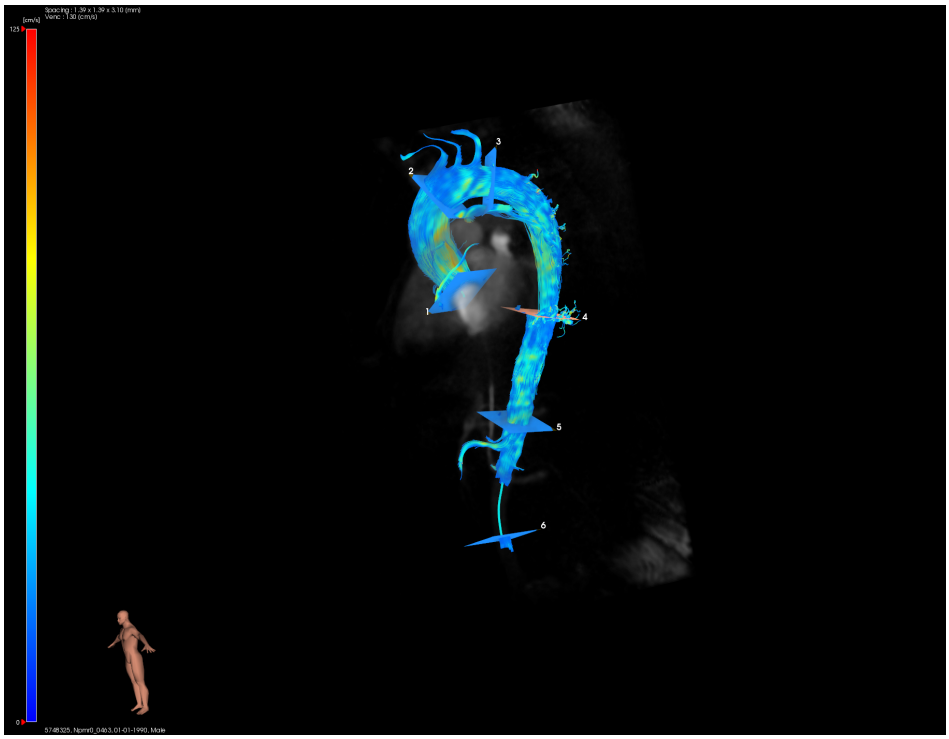

Figure 19: MRI scan used in the research of patient 0463.

As illustrated in Figure 19, each patient has their flow rate measured at various planes with a trigger delta ranging from $29 - 38$s, the first plane is at the beginning of the Ascending Aorta. At peak systolic cardiac phase (t_{p}), the time when the variation of 3D speed of the entire MRI data set is greatest, the area of the planes are determined (A_{p}). Cubic spline interpolation in the time dimension is used to fit a curve through the flow data of the plane at the start of the Ascending Aorta. This curve is then used as inflow boundary condition.

As we are not dealing with forward prescription, the flow rate $Q_{in}(t)$ is forced using

$$A_0^{n+1} = A_0^n - \frac{\Delta t}{\Delta x}\left(\bar{u}_1^{n+1} A_1^{n+1} - Q_0^{n+1}\right) \tag{93}$$

where Q_0^{n+1} is $Q_{\text{in}}(t^{n+1})$. Velocity is then determined by $u_0^{n+1} = \frac{Q_0^{n+1}}{A_0^{n+1}}$.

9.1.2 Single-factor Scaling

The single-factor scaling method ensures that at t_{p}, when the MRI measure the cross-sectional area of the Ascending Aorta to be A_{p}, the model also returns A_{p}. To achieve this, the 1D model is run for 10 cycles to ensure a stable cycle. Afterwards, the last cycle is used to determine p_{d}, the diastolic pressure, at plane 1. We then also determine the pressure p_{p} at t_{p}.

We assume flow to be zero at (p_{d}), which in practice is a reasonable assumption. Equation (14) only holds when A_0 is determined at static equilibrium, meaning no flow. If this condition is met, it is also often written with a reference pressure, (p_{ref}) in our case, as

$$p = p_{\text{ext}} + p_{\text{ref}} + \beta(\sqrt{A} - \sqrt{A_d}) \tag{94}$$

See for example [3] and [2]. We now set p_{ref} to p_{d}.

Next, the Newton-Raphson method is used to find an A_{d}, the cross-sectional area of the Ascending Aorta at diastolic pressure, such that for area A_{p}, equation (94) returns p_{p}. The function that is minimized is given by

$$f = p_{\text{ext}} + p_{\text{d}} - p_{\text{t}} + \beta(A_{\text{d}})(\sqrt{A_{\text{p}}} - \sqrt{A_{\text{d}}}) \tag{95}$$

Which results in a new value for A_{d}. We now define

$$\psi = \frac{A_{\text{d,new}}}{A_{\text{d,old}}} \tag{96}$$

and multiply the dimensions of all arteries by ψ.
The model is now ran again to determine a new p_{d} and p_{p}. After a couple iterations, this method approaches a steady cycle. This ensures the agreement between the model and the MRI data that we want.
At the first run we take as initial guesses $p_{\text{t}} = 110$ mmHg and $p_{\text{d}} = 80$ mmHg. This method is repeated until the change in p_{t} and p_{d} is less than 1 mmHg.

9.1.3 Multi-factor Scaling

The goal of the multi-factor scaling method is to better match the dimensions of the scaled network to that of the MRI scan. The biggest difference between the single-factor scaled networks and the MRI data is the amount the cross-section of the aorta decreases in the Descending Thoracic Aorta (DTA). In the baseline model the cross-section at the beginning of the DTA is 2.5 times greater than at the end of the DTA. In the MRI data this tapering (decreasing of the cross-section of an artery) was less.
When performing the multi-factor scaling we also measure p_{p} at t_{p} at plane 3 (begin DTA) and plane 5 (end DTA). We now determine A_{d} for these two planes and also define

$$\psi_{\mathrm{plane}} = \frac{A_{\mathrm{d,plane,new}}}{A_{\mathrm{d,plane,old}}} \tag{97}$$

for each plane. We then multiply all arteries distal to plane 5 by $\frac{\psi_5}{\psi_3}$ to account for the lesser tapering.

9.1.4 Outflow conditions

We also need to perform scaling of the outflow conditions. For the scaling of R_{vb}, we define

$$\kappa = \frac{Z_{\mathrm{1D,new}}}{Z_{\mathrm{1D,old}}} \tag{98}$$

for every terminal vessel and multiply R_{vb} by κ. Since Z_{1D} and R_{vb} both have the same unit this is a viable scaling factor.

For C, we note that the compliance of a vessel can be estimated by

$$C_{\mathrm{v}} = \frac{1}{\rho} \cdot \int_0^l \frac{A_d}{c_d^2} dx \tag{99}$$

as in [2, 3], where l denotes the length of the vessel and c_d^2 is given by equation (16), where r_0 is replaced by r_d. We simplify and look at an artery with constant A_d. Then we define

$$\gamma = \frac{C_{\mathrm{v,new}}}{C_{\mathrm{v,old}}} = \frac{\frac{A_{\mathrm{d,new}}}{c^2_{\mathrm{d,new}}}}{\frac{A_{\mathrm{d,old}}}{c^2_{\mathrm{d,old}}}} \tag{100}$$

for every terminal vessel and then multiply C by γ.

9.1.5 Validation

To investigate the model performance, the flow at distal planes in the aorta is compared with the model output at these locations. After the MRI scan, the pressure in the right and left arm were also measured for each patient. These values, although not determined simultaneously with the MRI scan, will also be used to compare with the pressure results of the model.

There are two patients who have two bifurcation in the aortic arc instead of three. This is deemed to be a too large deviation from our baseline network to be able to make a meaningful comparison and these patients are thus not investigated.

9.2 Results

9.2.1 Patient 1 - 0463

The data is from patient 0463 in the supplemental file. The cross-section at the beginning of the DTA is around 1.74 larger than at the end of the DTA. We will first show results for the single-factor scaling method. Results for the pressure at the beginning of the Left and Right Brachial Artery and flow at the beginning and the end of the Ascending Aorta and the Descending Thoracic Aorta are shown in Figure 20. Observing the flow, we see that the flow from the model output and from the MRI data is exactly the same at the start of the Ascending Aorta since this is the inflow boundary condition. At the end of the Ascending Aorta there already is a small difference. We see that the model retains the same shape whilst the shape from the MRI data changes. This indicates that the MRI data is not perfect and has an error. At the start of the Descending Thoracic Aorta the flow shape is still the same, however the flow in the model is a bit lower. At the end of the Thoracic the flow in the model is substantially lower, this is exactly where the tapering takes place.

The results for the pressure in the left and right arm are summarized in Table 2.

Table 2: Results for the pressure in the left and right arm for patient 1.

	Left arm		Right arm	
	Measured	Model	Measured	Model
Heart rate (bpm)	44	48	45	48
Diastolic pressure (mmHg)	75	72	70	72
Systolic pressure (mmHg)	134	144	124	143

The fact that the pressure measurements were taken at a different time than the MRI scan makes comparing harder. Ignoring this complication, We see that the model produces comparable results to the measurement for the diastolic pressure. The systolic pressure is a bit higher in the model output. There is also a difference between systolic pressure for the right and left arm in the model but this is not as substantial as was measured.

Next, the results of the multi-factor scaling method are discussed. Results for the pressure at the beginning of the Left and Right Brachial Artery and flow at the beginning and end of the Descending Thoracic Aorta are shown in Figure 21. We have excluded the flow values at the Ascending Aorta as those are in high agreement with each other. As we can see from Figure 21, the flow values are better matched than the single-factor scaling method. This is to be expected as a wider artery means more room for the blood to flow through, thus a higher blood flow.

The pressure is vastly underestimated however. The widening of the aorta has created more room for the blood to flow through. Thus the overall pressure is significantly lower. If we only apply a widening, it is only logical to see a drop in pressure. By only scaling one part of the network, we have disrupted the way the network interacts with itself. If we were to scale the network correctly, we would need to know the dimensions of all arteries (or at least for a few generations of bifurcations).

We conclude that there is not enough information to perform a multi-factor scaling of the network. In fact, having enough information to perform a multi-factor scaling probably means having enough information to build a whole new network. This defeats the purpose of using a baseline network to not have to collect all this information. The single-factor scaling method thus seems to be preferable as it leaves the inner-workings of the network intact. We will investigate the method further for different patients.

To illustrate the propagation of pressure and velocity in the blood vessels, we have made a plot of the whole network at different times, which is shown in Figure 22. Figure 22 is constructed by representing each individual cell as an edge in a graph. That edge is then coloured by assigning a colour to its pressure value. Thus, Figure 24 shows the pressure in all 4600 cells. The representation is not up to scale. This kind of visualisation, which is novel to our understanding, makes it easy to see how the pressure propagates and allows for a better understanding of the underlying dynamics than the static plots that were used so far.

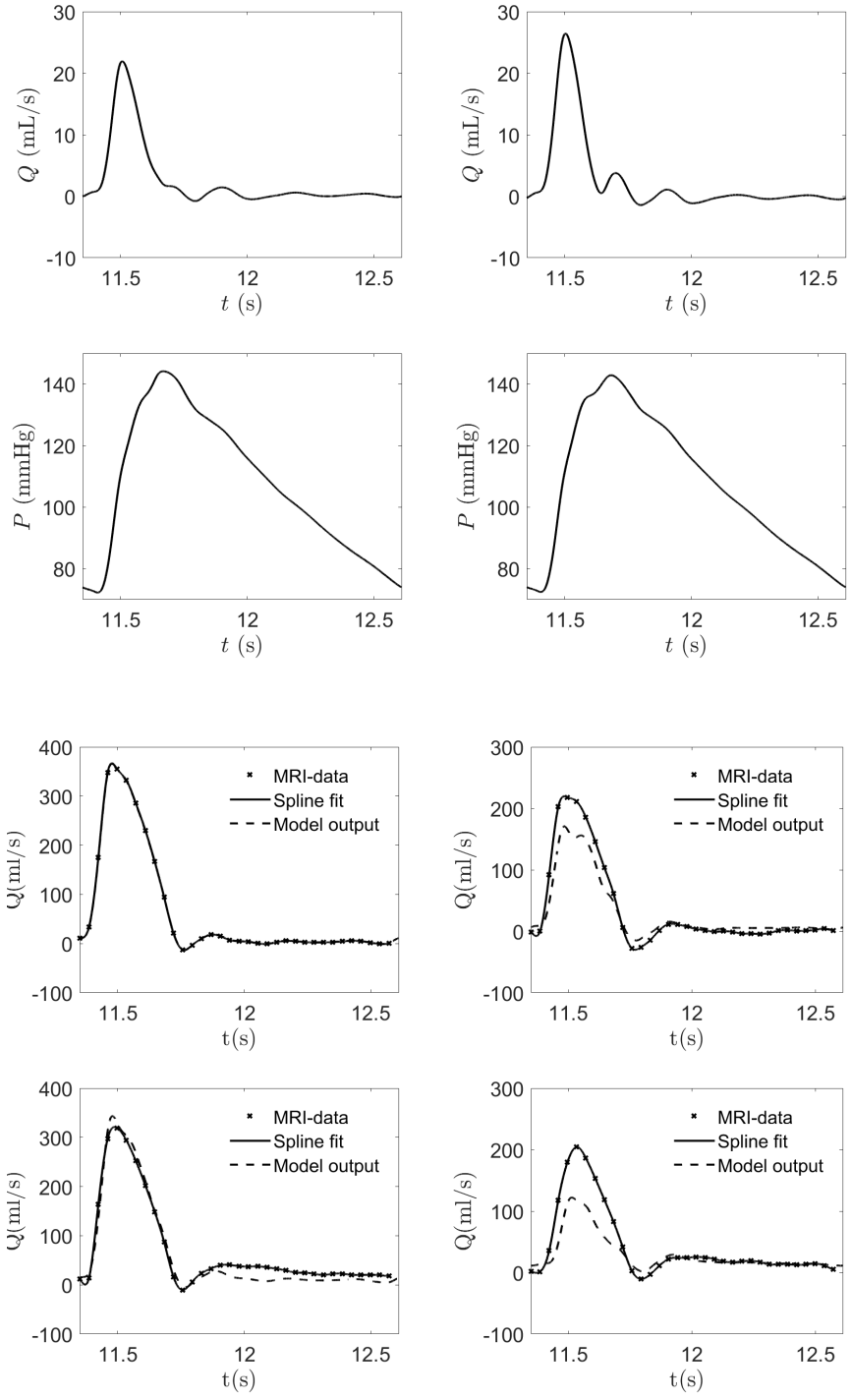

Figure 20: Results for the first patient (0463) using the single-factor scaling method. Top, from left to right: flow and pressure at the Left Brachial and Right Brachial. Bottom left, flow at the beginning (top) and end of the Ascending Aorta (bottom). Bottom right, flow at the beginning (top) and end of the Descending Thoracic Aorta (bottom).

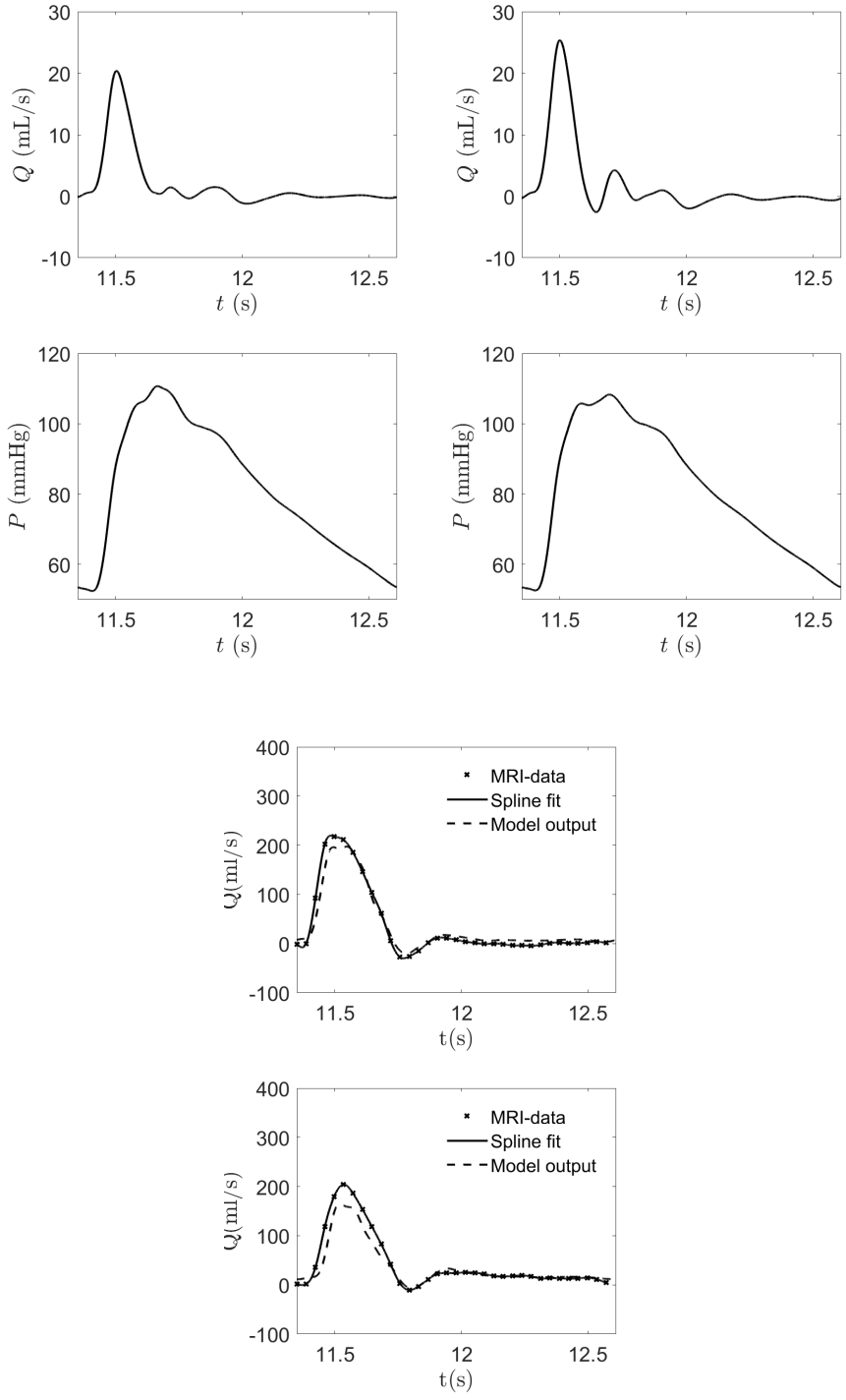

Figure 21: Results for the first patient (0463) using the multi-factor scaling method. Top, from left to right: flow and pressure at the Left Brachial and Right Brachial. Bottom, flow at the beginning (top) and end of the Descending Thoracic Aorta (bottom).

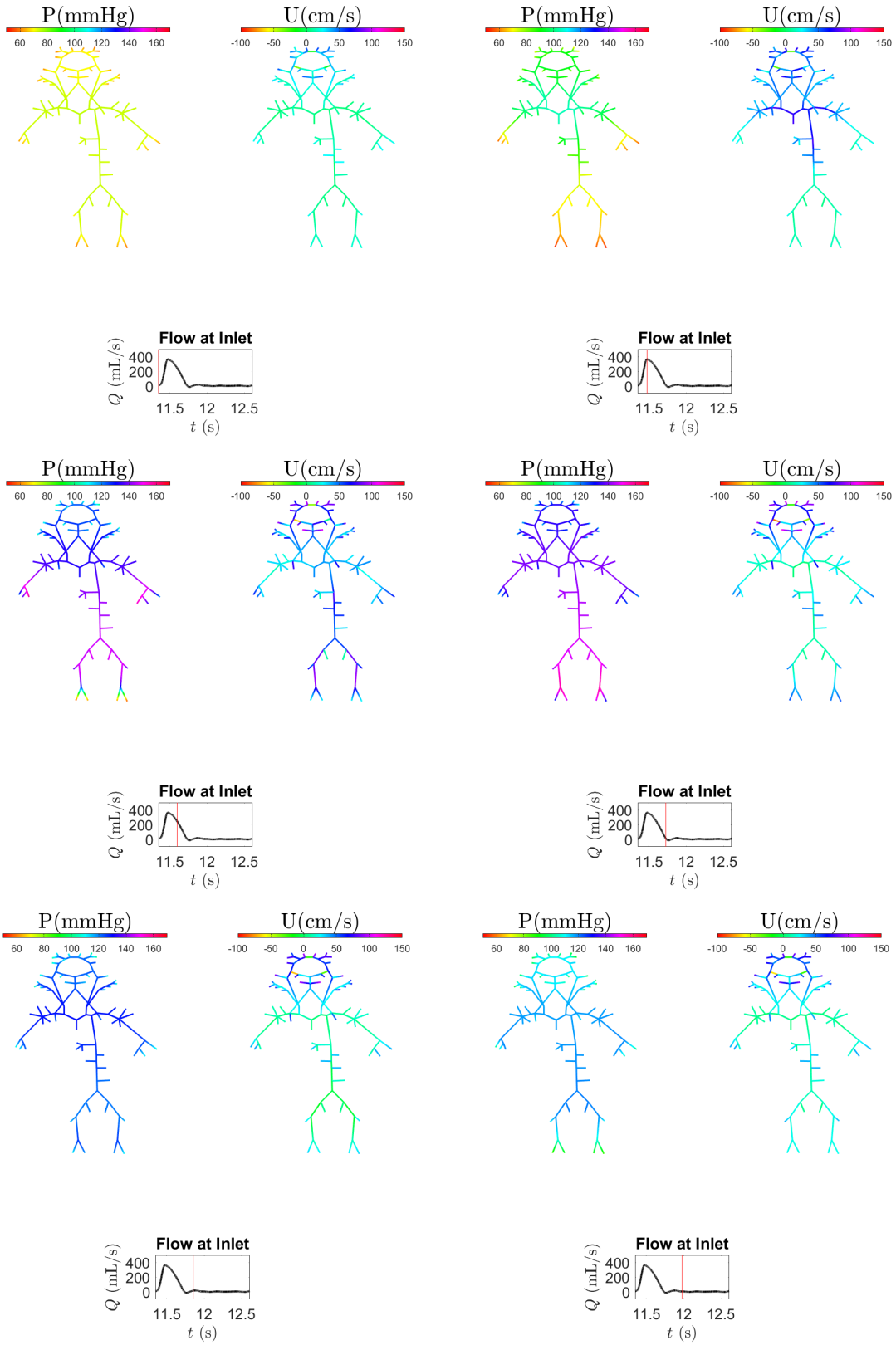

Figure 22: Visual representation of pressure and velocity propagation in the full 111-artery network for patient 0463. From left to right, first row $t = 11.35$ s and $t = 11.48$ s. Second row $t = 11.60$ s and $t = 11.73$ s. Third row $t = 11.85$ s and $t = 11.98$ s.

9.2.2 Patient 2 - 0314

Here we only applied the single-factor method. In the supplemental file, this data is from patient 0314. The cross-section at the beginning of the DTA is around 1.76 larger than at the end of the DTA. Results for the pressure at the beginning of the Left and Right Brachial Artery and flow at the beginning and end of the Descending Thoracic Aorta are shown in Figure 23.
Firstly, the flow at the beginning of the Descending Thoracic Aorta has roughly the same shape and magnitude as the MRI data. At the end of the Descending Thoracic Aorta the model output again has a lower flow due to the tapering. It still is in reasonable agreement however.

The results for the pressure are summarized in Table 3.

Table 3: Results for the pressure in the left and right arm for patient 2.

	Left arm		Right arm	
	Measured	Model	Measured	Model
Heart rate (bpm)	64	73	67	73
Diastolic pressure (mmHg)	91	92	85	92
Systolic pressure (mmHg)	144	144	138	143

From Table 3 we can conclude that the model makes a reasonable prediction of the overall pressure and the pressure drop in the left and right arm. It is hard to say what the effect of the difference in heart rate is, since the heart rate is higher when measuring the right arm pressure, but the determined pressure is lower, which one might not expect.

In this patient the aorta is less tapered and the model better predicted flow and pressure. It seems that having a baseline network that has the same ratios as the patient results in better predictions. With the errors in MRI measurement and uncertainties when measuring the pressures in both arms in mind, we can conclude that the 1D model produces reasonable results. Its output can not be used to perform precise predictions. However, it does capture the overall shape and magnitude of flow and pressure wave forms. A colour plot of the blood pressure and velocity is shown in Figure 24.

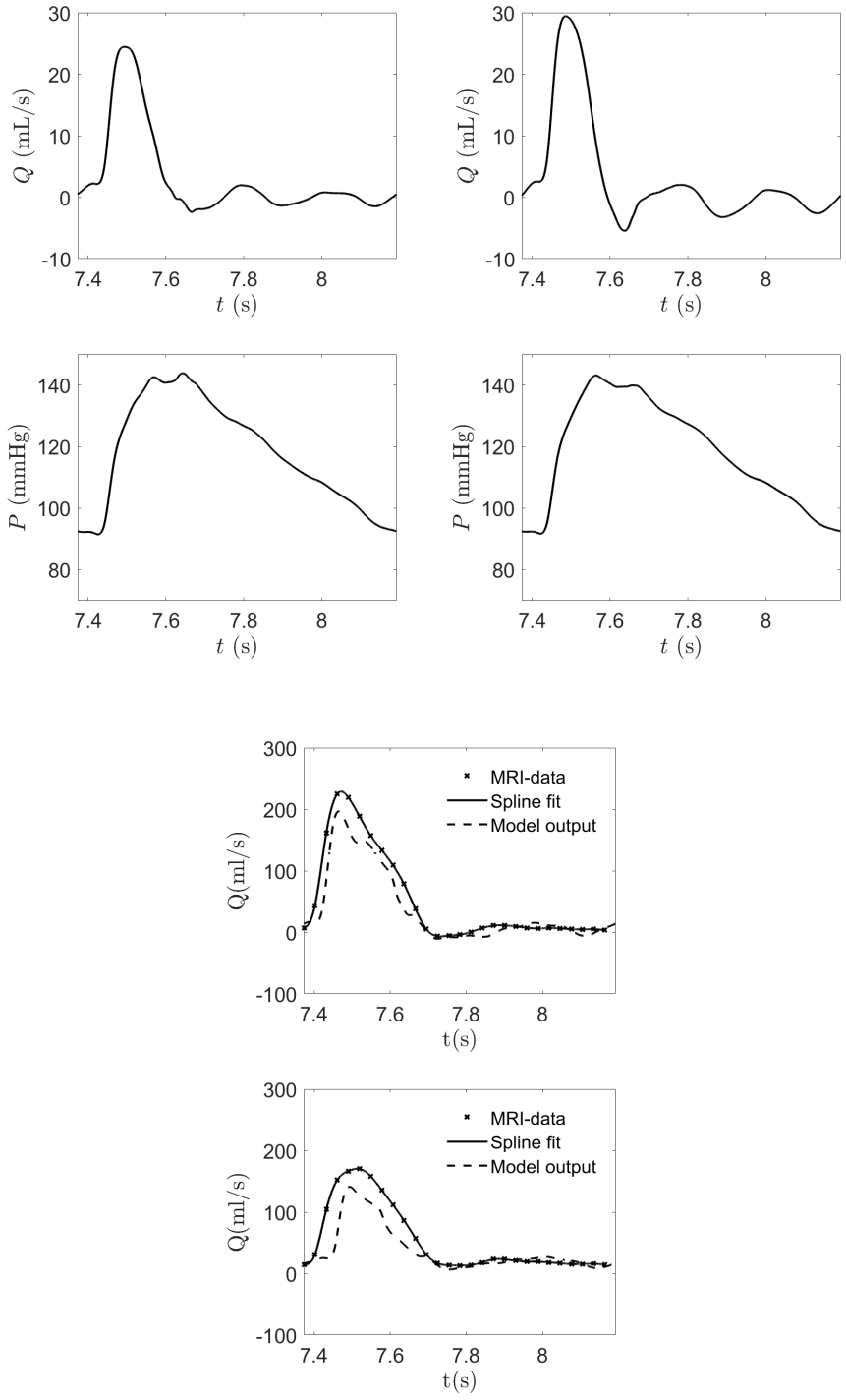

Figure 23: Results for the second patient 0314. Top, left to righ: flow and pressure at the Left Brachial and right Right Brachial. Bottom, flow at the beginning (top) and end of the Descending Thoracic Aorta (bottom).

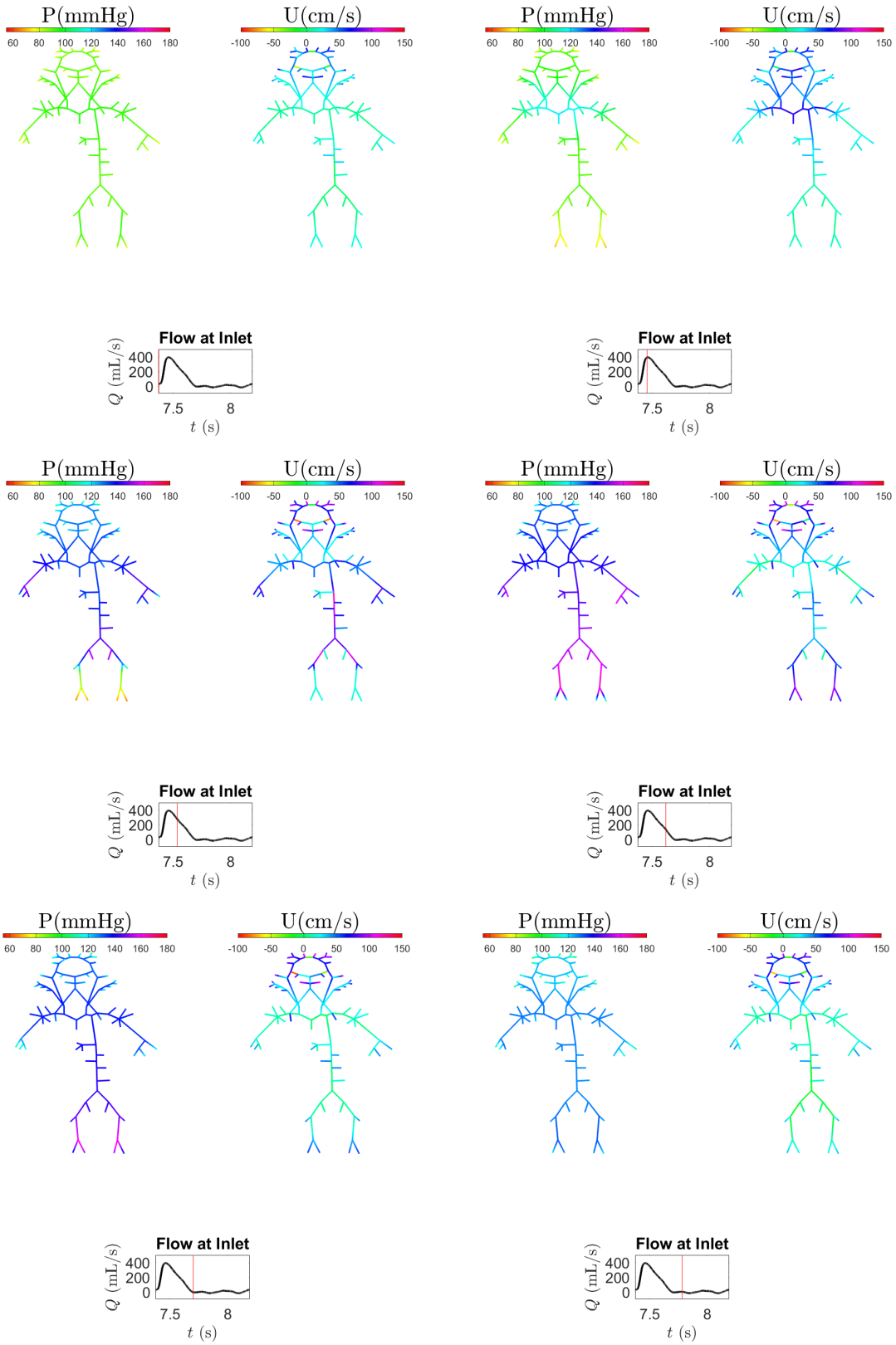

Figure 24: Visual representation of pressure and velocity propagation in the full 111-artery network for patient 0314. From left to right, first row $t = 7.37$ s and $t = 7.45$ s. Second row $t = 7.54$ s and $t = 7.62$ s. Third row $t = 7.70$ s and $t = 7.78$ s.

9.2.3 Patient 3 - 0215

This concerns the data from patient 0215 in the supplemental file. The cross-section at the beginning of the DTA is around 1.74 larger than at the end of the DTA. The diastolic pressure in the left and right arm is around 60 mmHg whilst the systolic pressure is around 90 mmHg. This hints at hypotension (low blood pressure). To account for this, we experimentally set β to 0.7 of its original value. Results are shown in Figure 25
Results for the pressure are summarized in Table 4.

Table 4: Results for the pressure in the left and right arm for patient 3.

	Left arm		Right arm	
	Measured	Model	Measured	Model
Heart rate (bpm)	67	61	56	61
Diastolic pressure (mmHg)	62	56	60	56
Systolic pressure (mmHg)	93	99	92	97

We again see an underestimation of flow and a relatively comparable pressure value. A colour plot is given in Figure 26.

From our results we can conclude that the single-scaling factor estimates pressure in the left and right arm with reasonable accuracy. Depending on the patient, it underestimates the flow in the distal part of the aorta. Patient 2 has the best estimation of flow and pressure simultaneously, indicating a correlation between the two. It is probable that if our baseline network had a lesser tapered aorta, the flow in the aorta and thus the pressure in the arm of patient 1 and 3 would have been better estimated by the model. Research into a baseline model with a lesser tapering of the aorta is therefore desirable. One can imagine a system where a few key characteristics of a patient, for example having three or two bifurcation in the aortic arch and the amount of tapering of the aorta, are determined. Then, a baseline model is selected with the same characteristics as the patient. This would require a handful of detailed arterial networks, each with its own unique combination of characteristics, to be documented. This way accurate non-invasive and multi-location pressure prediction would be possible for a high number of patients with only a single MRI scan. Patient 3 shows us that the model can be adapted to account for diseased states.

The combination of a well-matched baseline model, MRI scan data and the colour plots can give an accurate and easily understandable representation of the pressure propagation in an individual patient.

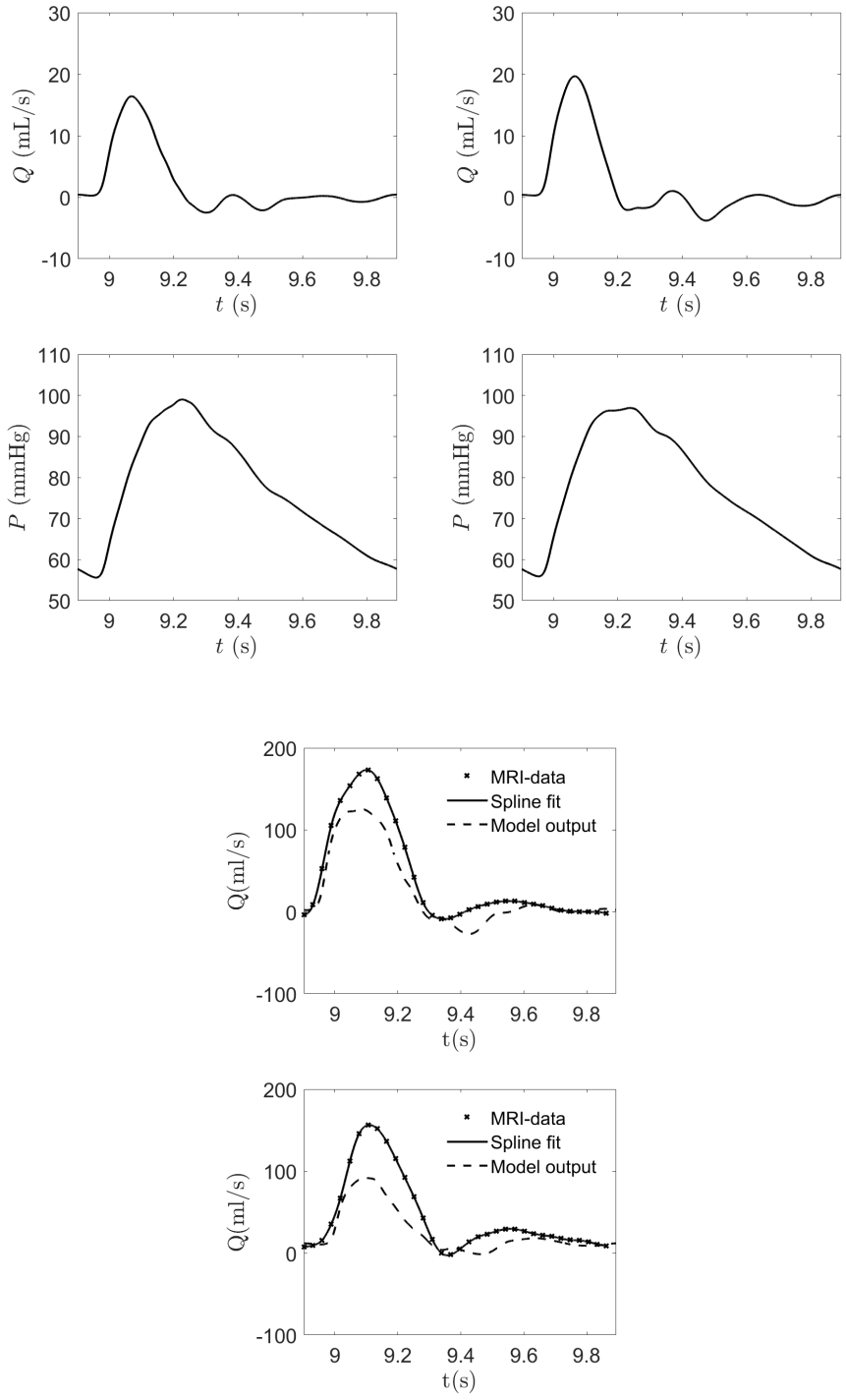

Figure 25: Results for the third patient 0215. Top, from left to right: flow and pressure at the Left Brachial and Right Brachial. Bottom, flow at the beginning(top) and end of the Descending Thoracic Aorta (bottom).

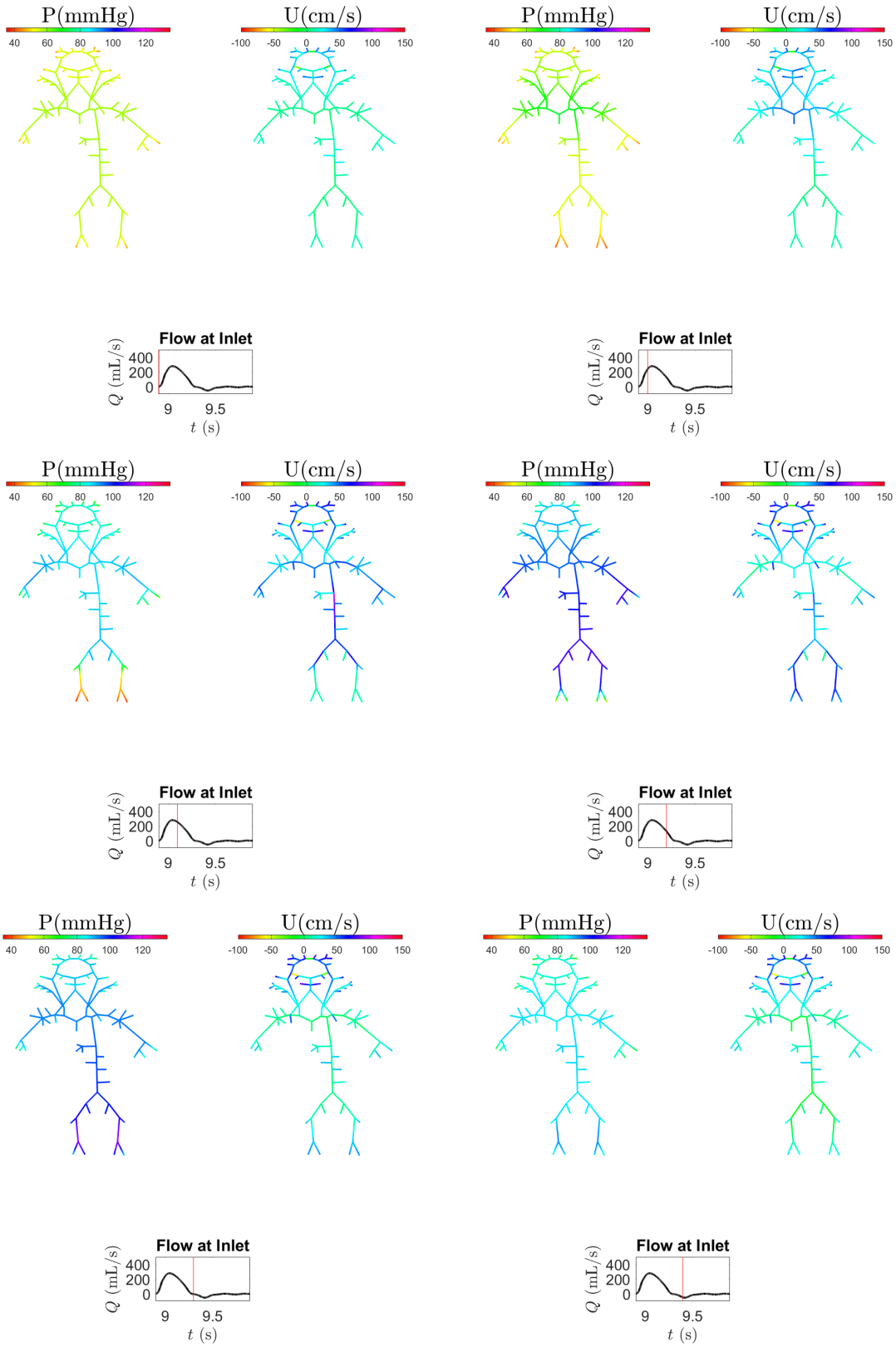

Figure 26: Visual representation of pressure and velocity propagation in the full 111-artery network for patient 0215. From left to right, first row $t = 8.90$ s and $t = 9.00$ s. Second row $t = 9.10$ s and $t = 9.20$ s. Third row $t = 9.30$ s and $t = 9.40$ s.

10 Conclusions

We will structure our conclusions in the following way. First, a list is given that details the changes to the model of Rozendaal [7]. Then the validation of the model is discussed. Next, the results of the scaled model combined with the MRI data is discussed. Finally, recommendations for future work are presented.

The changes to the model of [7] are presented.

- The treatment of bifurcations was changed.
- The model now includes the high resolution method at the branching points.
- The model now includes several types of branching points.
- The network was changed from a 55-artery to a 111-artery network.
- The inlet boundary condition was changed from a simple sinusoidal model to a more complicated model including prescribed ventricular pressure and a model for the aortic valve.
- The outlet boundary condition was changed from a reflection coefficient to a windkessel model.
- The model implementation was made roughly 10 times faster by including sparse matrices.

It was shown that the high resolution flux difference splitting method combined with the new treatment of bifurcations produces highly comparable results to the Discontinuous Galerkin method from Sherwin et al. [15] in the 55-artery network with a simple sinusoidal heart model as inlet boundary condition and a terminal reflection coefficient as outlet boundary condition.
Next, a more extensive 111-artery network is studied. A heart model consisting of a prescribed ventricular pressure cycle and a heart valve that opens and closed based on local pressure/velocity conditions is used. The three-element windkessel model, an analogy from electric circuits, is used as an outflow boundary condition. The high resolution flux difference splitting method proved to be capable of producing results highly comparable to a more elaborate closed loop model from Mynard and Smolich [10] and to *in vivo* measurements.

The one-dimensional model with the 111-artery network as a baseline network is combined with MRI scan results obtained at the Leids Univesitair Medisch Centrum (LUMC) to investigate its capability of predicting pressure and flow wave forms in individual patients. The novel aspects of this approach are represented.

- The use of MRI acquired flow data as inflow boundary condition.
- The use of a scaling method to conform the dimensions of the model with that of the MRI scan.
- The use of a scaling method for the outlet boundary conditions.
- The use of the colour plots to present results.

The flow measured at the inlet of the Ascending Aorta with the MRI scan is used as the inflow boundary condition. To make the model partially patient-specific, two types of scaling method are researched. With the single-factor scaling method, the model is scaled such that the area of the Ascending Aorta in the model equals the area determined at the LUMC at the time of measurement. Outlet boundary conditions were scaled accordingly. With the multi-factor scaling method, the tapering of the aorta, meaning the amount it decreases in size further from the heart, in the baseline model is reduced to better match LUMC measurements, all arteries distal to this tapering were also scaled. The results were compared with flow measurements at various locations in the aorta and pressure measurements in the right and left arm.
The multi-factor scaling proved incapable of producing realistic pressure results despite producing realistic flow results. It can be concluded that a multi-factor scaling can only be applied to change local dimensions of the network and not global dimensions as this changes the characteristics of the network too much.

It was shown that the model is capable of producing realistic results for an individual patient with a single-factor scaling method and that the accuracy of these results in all probability depends on the agreement of the ratios of the baseline network and the arterial network of the patient. The single-factor scaling is combined with a novel colour plot of the entire network to show pressure and velocity propagation in the 111-artery network of the patient in the MRI scan. A high agreement of ratios between the baseline network and the arterial network of the patient could lead to accurate non-invasive, multi-location pressure prediction.

Following are recommendations for future study. The recommendations concerning the mathematical basis for the study are represented.

- Including a more sophisticated pressure-area relation.
- Including a more sophisticated description of the frictional force by assuming a different velocity profile.
- Changing the blood density to $1.06\ \mathrm{g/cm^3}$ which is a more widely used value.
- Researching the effect of including gravitational forces.

All the previous recommendations stand to improve the model. We should stress however, that the acquired results show that the model is already accurate. Since the application in this paper is novel and has a lot of potential, it may be of more interest to pursue this path of further research. The recommendations concerning the development of partially patient-specific models are represented.

- Expanding the number of patients analysed using the 111-artery network.
- Documenting a handful of detailed arterial networks, each with its own unique combination of characteristics, to be used for scaling.
- Research into modelling patients with a diseased aorta with the possibility of using a multi-factor scaling method to change local dimensions (a local bulge in the aorta for example).

References

[1] Mitran S Rossmanith J. Bale D, LeVeque R. A wave propagation method for conservation laws and balance laws with spatially varying flux functions. *SIAM Journal on Scientific Computing.*, 24(3):955–978, 2003.

[2] Chowienczyk PJ Alastruey J. Epstein S, Willemet M. Reducing the number of parameters in 1d arterial blood flow modelling: less is more for patient specific simulations. *Am. J. Physiol. Heart Cir. Physiol.*, 2015.

[3] Alastruey J Hellevik LR. Fossan FE, Mariscal-Harana J. Optimization of topological complexity for one-dimensional arterial blood flow models. *J. R. Soc. Interface*, 2018.

[4] Mynard J. One-dimnesional blood flow modelling with the locally conservative galerkin (lcg) method., 2007.

[5] Mynard J. *Computer modelling and wave intensity analysis of perinatal cardiovascular function and dysfunction.* PhD thesis, The University of Melbourne, Melbourne, Australia, 2011.

[6] Liu X. Lax P. Solution of two-dimensional riemann problems of gas dynamics by positive schemes. *SIAM Journal on Scientific Computing*, 19(2):319–340, 1998.

[7] Rozendaal M. One-dimensional blood flow modelling in the human arterial system with finite volume methods., 2017.

[8] Xenos M. Malatos S, Raptis A. Advances in low-dimensional mathematical modeling of the human cardiovascular system. *J Hypertens Manag*, 2016.

[9] Olufsen MS. Structured tree outflow condition for blood flow in larger systemic arteries. *Am. J. Physiol. Heart Cir. Physiol*, 1999.

[10] Smolich J. Mynard J. One-dimensional haemodynamic modeling and wave dynamics in the entire adult circulation. *Annals of Biomedical Engineering.*, 43(6):1443–1460, 2015.

[11] Frank O. Die grundform des arteriellen pulses: Mathematische analyse. *Zeitschrift für Biologie*, 1899.

[12] Joaquim Peiro, Spencer Sherwin, K Parker, V. Franke, Luca Formaggia, Daniele Lamponi, and Alfio Quarteroni. Numerical simulation of the arterial pulse propagation using one-dimensional models. 01 2003.

[13] LeVeque R. *Finite Volume Methods For Hyperbolic Problems.* Cambridge Univ.Press, Cambridge, 2011.

[14] H.-H. Sievers R.G. Leyh, C. Schmidtke and M.H. Yacoub. Opening and closing characteristics of the aortic valce after different types of valve-preserving surgery. *Circulation.*, 100(21):2153–2160, 1999.

[15] Peiro J Franke V. Sherwin S, Formaggia L. Computational modelling of 1d blood flow with variable mechanical properties and its application to the simulation of wave propagation in the human arterial system. *International Journal for Numerical Methods in Fluids.*, pages 673–700, 2003.

[16] D. F. Young Stergiopulos, N. and T. R. Rogge. Computer simulation of arterial flow with applications to arterial and aortic stenoses. *J. Biomech.*, pages 1477–1488, 1992.

A CGS conversion table

In Table 5, the conversion from CGS units to SI units is shown.

Table 5: Conversion Table for the CGS system to SI units.

Quantity	CGS unit	Definition	SI
length	centimetre (cm)	1 / 100 of metre	$=10^{-2}\mathrm{m}$
mass	gram (g)	1 / 1000 of kilogram	$=10^{-3}\mathrm{kg}$
time	second (s)	1 second	=1 s
velocity	centimetre per second (cm/s)	cm / s	$=10^{-2}\mathrm{m/s}$
acceleration	gal (Gal)	cm / s^2	$=10^{-2}\mathrm{m/s}^2$
force	dyne (dyn)	g $\cdot\mathrm{cm/s}^2$	$=10^{-5}\mathrm{N}$
energy	erg (erg)	g $\cdot\mathrm{cm}^2/\mathrm{s}^2$	$=10^{-7}\mathrm{J}$
power	erg per second (erg/s)	g $\cdot\mathrm{cm}^2/\mathrm{s}^3$	$=10^{-7}\mathrm{W}$
pressure	barye (Ba)	g / cm $\cdot\mathrm{s}^2$	$=10^{-1}\mathrm{Pa}$
dynamic viscosity	poise (P)	g / cm $\cdot$s	$=10^{-1}\mathrm{Pa}\cdot\mathrm{s}$
kinematic viscosity	stokes (St)	cm^2/s	$=10^{-4}\mathrm{m}^2/\mathrm{s}$

B Physiological data for the 55 arteries

The physiological data from Sherwin et al. [15] for the 55 arteries are shown in Table 6 and in Table 7.

Table 6: Physiological data for the 55 arteries from [15] (1).

#	Artery	Length (cm)	Area (cm^2)	β($kg\ s^{-2}\ cm^{-2}$)	R_t
1	Ascending Aorta	4.0	5.983	97	—
2	Aortic Arch I	2.0	5.147	87	—
3	Brachiocephalic	3.4	1.219	233	—
4	R. Subclavian I	3.4	0.562	423	—
5	R. Carotid	17.7	0.432	516	—
6	R. Vertebral	14.8	0.123	2590	0.906
7	R. Subclavian II	42.2	0.510	466	—
8	R. Radial	23.5	0.106	2866	0.82
9	R. Ulnar I	6.7	0.145	2246	—
10	R. Interosseous	7.9	0.031	12894	0.956
11	R. Ulnar II	17.1	0.133	2446	0.893
12	R. Internal Carotid	17.6	0.121	2644	0.784
13	R. External Carotid	17.7	0.121	2467	0.79
14	Aortic Arch II	3.9	3.142	130	—
15	L. Carotid	20.8	0.430	519	—
16	L. Internal Carotid	17.6	0.121	2644	0.784
17	L. External Carotid	17.7	0.121	2467	0.791
18	Thoracic Aorta I	5.2	3.142	124	—
19	L. Subclavian I	3.4	0.562	416	—
20	Vertebral	14.8	0.123	2590	0.906
21	L. Subclavian II	42.2	0.510	466	—
22	L. Radial	23.5	0.106	2866	0.821
23	L. Ulnar I	6.7	0.145	2246	—
24	L. Interosseous	7.9	0.031	12894	0.956
25	L. Ulnar II	17.1	0.133	2446	0.893
26	Intercostals	8.0	0.196	885	0.627
27	Thoracic Aorta II	10.4	3.017	117	—
28	Abdominal I	5.3	1.911	167	—
29	Celiac I	2.0	0.478	475	—
30	Celiac II	1.0	0.126	1805	—
31	Hepatic	6.6	0.152	1142	0.925
32	Gastric	7.1	0.102	1567	0.921
33	Splenic	6.3	0.238	806	0.93
34	Superior Mesenteric	5.9	0.430	569	0.934
35	Abdominal II	1.0	1.247	227	—
36	L. Renal	3.2	0.332	566	0.861
37	Abdominal III	1.0	1.021	278	—
38	R. Renal	3.2	0.159	1181	0.861
39	Abdominal IV	10.6	0.697	381	—
40	Inferior Mesenteric	5.0	0.080	1895	0.918
41	Abdominal V	1.0	0.578	399	—
42	R. Common Iliac	5.9	0.328	649	—
43	L. Common Iliac	5.8	0.328	649	—
44	L. External iliac	14.4	0.252	1493	—
45	L. Internal Iliac	5.0	0.181	3134	0.925
46	L. Femoral	44.3	0.139	2559	—
47	L. Deep Femoral	12.6	0.126	2652	0.885
48	L. Posterior Tibial	32.1	0.110	5808	0.724
49	L. Anterior Tibial	34.3	0.060	9243	0.716

Table 7: Physiological data for the 55 arteries from [15] (2).

#	Artery	Length (cm)	Area (cm^2)	β ($kg\ s^{-2}\ cm^{-2}$)	R_t
50	R. External Iliac	14.5	0.252	1493	—
51	R. Internal Iliac	5.1	0.181	3134	0.925
52	R. Femoral	44.4	0.139	2559	—
53	R. Deep Femoral	12.7	0.126	2652	0.888
54	L. Posterior Tibial	32.2	0.110	5808	0.724
55	R. Anterior Tibial	34.4	0.060	9243	0.716

C Physiological data for the 111 arteries

The physiological data from Mynard and Smolich [10] for the 11 arteries are shown in Table 8, Table 9 and Table 10.

Table 8: Physiological data for the 111 arteries from [10] (1).

	Segment Name	Segment Abbreviation	Length (cm)	Inlet A, (cm^2)	Outlet A, (cm^2)	Inlet connects To	Outlet connects to
Systemic Arteries							
1	Ascending Aorta	AscAo	4.0	6.7887	6.7887	Boundary	AoArc(I), BCA
2	Aortic Arch I	AoArc(I)	2.0	5.2279	5.2279	AscAo	AoArc(II), LCA
3	Brachiocephalic Artery	BCA	3.4	1.5350	1.5350	AscAo	RCA, RSub(I)
4	Right Subclavian Artery I	RSub(I)	3.4	1.1310	0.9503	BCA	RVertI, RIntTh, RSub(II)
5	Right Carotid Artery	RCA	9.4	0.5027	0.3739	BCA	RICA, RECA(I)
6	Right Vertebral Artery	RVert	14.9	0.1075	0.0616	RSub(I)	Bas(II)
7	Right Internal Thoracic Artery	RIntTh	8.0	0.0661	0.0661	RSub(I)	VB:Chest
8	Right Subclavian Artery II	RSub(II)	2.5	0.9503	0.9503	RSub(I)	RThyrc, RAxill
9	Right Thyrocervical Artery	RThyrc	5.0	0.1662	0.1662	RSub(II)	VB:RShoulder
10	Right Axillary Artery	RAxill	5.0	0.8992	0.8992	RSub(II)	RSubsc, RBrach
11,12,13,14	Right Subscapular Artery etc [x4]	RSubsc	4.0	0.1134	0.1134	RAxill	VB:RShoulder
15	Right Brachial Artery	RBrach	34.7	0.6082	0.1750	RAxill	RRad, RUlnar(I)
16	Right Radial Artery	RRad	23.5	0.0531	0.0362	RBrach	VB:RArm
17	Right Ulnar Artery I	RUlnar(I)	6.7	0.1452	0.1452	RBrach	RInter, RUlnar(II)
18	Right Interosseous Artery	RInter	7.9	0.0260	0.0260	RUlnar(I)	VB:RArm
19	Right Ulnar Artery II	RUlnar(II)	17.1	0.1257	0.1052	RUlnar(I)	VB:RArm
20	Right Internal Carotid Artery	RICA	17.8	0.2552	0.1452	RCA	RICASin, ROpth
21	Right External Carotid Artery I	RECA(I)	4.1	0.1963	0.1590	RCA	RECA(II), RSupThy
22	Aortic Arch II	AoArc(II)	3.9	4.8305	4.8305	AoArc(I)	DTA(I), LSub(I)
23	Left Carotid Artery	LCA	13.9	0.4301	0.3267	AoArc(I)	LICA, LECA(I)
24	Left Internal Carotid Artery	LICA	17.8	0.2206	0.1320	LCA	LIntCarSin, LOpth
25	Left External Carotid Artery I	LECA(I)	4.1	0.1735	0.1452	LCA	LExtCar(II), LSupThy
26	Descending Thoracic Aorta	DTA	15.6	3.8013	1.5837	AoArc(II)	AbdAo(I), Cel
27	Left Subclavian Artery I	LSub(I)	3.4	0.9503	0.7854	AoArc(II)	LVert, LIntTh, LSub(II)
28	Left Vertebral Artery	LVert	14.8	0.1075	0.0616	LSub(I)	Bas(II)
29	Left Internal Thoracic Artery	LIntTh	8.0	0.0573	0.0573	LSub(I)	VB:Chest
30	Left Subclavian Artery II	LSub(II)	2.5	0.6793	0.6793	LSub(I)	LThyrc, LAxill
31	Left Thyrocervical Artery	LThyrc	5.0	0.1075	0.1075	LSub(II)	VB:LShoulder
32	Left Axillary Artery	LAxill	5.0	0.6362	0.6362	LSub(II)	LSubsc, LBrach
33,34,35,36	Left Subscapular Artery etc [x4]	LSubsc	4.0	0.0804	0.0804	LAxill	VB:LShoulder
37	Left Brachial Artery	LBrach	34.7	0.5102	0.1750	LAxill	LRadI, LUlnar(I)
38	Left Radial Artery	LRad	23.5	0.0531	0.0362	LBrach	VB:LArm
39	Left Ulnar Artery I	LUlnar(I)	6.7	0.1452	0.1452	LBrach	LInter, LUlnar(II)
40	Left Interosseous Artery	LInter	7.9	0.0260	0.0260	LUlnar(I)	VB:LArm
41	Left Ulnar Artery II	LUlnar(II)	17.1	0.1257	0.1052	LUlnar(I)	VB:LArm
42	Abdominal Aorta I	AbdAo(I)	5.3	1.1690	1.1690	DTA	SupMes, AbdAo(II)
43	Celiac Artery	Cel	2.0	0.4536	0.4536	DTA	Hep, Spl, Gas
44	Hepatic Artery	Hep	6.6	0.1810	0.1810	Cel	VB:Liver
45	Splenic Artery	Spl	6.3	0.1257	0.1257	Cel	VB:Spleen
46	Gastric Artery	Gas	7.1	0.2642	0.2376	Cel	VB:Stomach
47	Superior Mensenteric Artery	SupMes	5.9	0.2827	0.2827	AbdAo(I)	VB:Intestines
48	Abdominal Aorta II	AbdAo(II)	1.0	1.0936	1.0936	AbdAo(I)	LRenal, AbdAo(III)
49	Left Renal Artery	LRenal	3.2	0.2124	0.2124	AbdAo(II)	VB:LKidney
50	Abdominal Aorta III	AbdAo(III)	1.0	1.0207	1.0207	AbdAo(II)	RRenal, AbdAo(IV)

Table 9: Physiological data for the 111 arteries from [10] (2).

51	Right Renal Artery	RRenal	3.2	0.2124	0.2124	AbdAo(III)	VB:RKidney
52	Abdominal Aorta IV	AbdAo(IV)	10.6	0.9503	0.8825	AbdAo(III)	InfMes, AbdAo(V)
53	Inferior Mesenteric Artery	InfMes	5.0	0.0804	0.0804	AbdAo(IV)	VB:Intestines
54	Abdominal Aorta V	AbdAo(V)	1.0	0.8495	0.7854	AbdAo(IV)	LCmIliac, RCmIliac
55	Left Common Iliac Artery	LCmIliac	5.9	0.4254	0.3848	AbdAo(V)	LExIliac, LInIliac
56	Right Common Iliac Artery	RCmIliac	5.8	0.4254	0.3848	AbdAo(V)	RExIliac, RInIliac
57	Left External Iliac Artery	LExIliac	14.4	0.2463	0.2290	LCmIliac	LFem, LDpFem
58	Left Internal Iliac Artery	LInIliac	5.0	0.2179	0.2179	LCmIliac	VB:Pelvis
59	Left Femoral Artery	LFem	44.3	0.1963	0.1134	LExIliac	LPTib, LATib
60	Left Deep Femoral Artery	LDpFem	12.6	0.0707	0.0489	LExIliac	VB:LUpLeg
61	Left Posterior Tibial Artery	LPTib	32.1	0.0755	0.0616	LFem	VB:LLowLeg
62	Left Anterior Tibial Artery	LATib	34.3	0.0531	0.0415	LFem	VB:LLowLeg
63	Right External Iliac Artery	RExIliac	14.5	0.2463	0.2290	RCmIliac	RFem, RDpFem
64	Right Internal Iliac Artery	RInIliac	5.0	0.2179	0.2179	RCmIliac	VB:Pelvis
65	Right Femoral Artery	RFem	44.4	0.1963	0.1134	RExIliac	RPTib, RATib
66	Right Deep Femoral Artery	RDpFem	12.7	0.0707	0.0489	RExIliac	VB:RUpLeg
67	Right Posterior Tibial Artery	RPTib	32.2	0.0755	0.0616	RFem	VB:RLowLeg
68	Right Anterior Tibial Artery	RATib	34.4	0.0531	0.0415	RFem	VB:RLowLeg
Head/Neck Arteries							
69	Basilar Artery II	Bas(II)	2.0	0.1257	0.1134	RVert, LVert	RSupCer, LSupCer, Bas(I)
70	Right Superior Cerebellar Artery	RSupCer	1.0	0.0227	0.0154	Bas(II)	VB:Brain
71	Left Superior Cerebellar Artery	LSupCer	1.0	0.0227	0.0154	Bas(II)	VB:Brain
72	Basilar Artery I	Bas(I)	0.5	0.0755	0.0573	Bas(II)	RPostCer(I), LPostCer(I)
73	Right Posterior Cerebral Artery I	RPostCer(I)	0.2	0.0284	0.0284	Bas(I)	RPostComm, RPostCer(II)
74	Left Posterior Cerebral Artery I	LPostCer(I)	0.2	0.0284	0.0284	Bas(I)	LPostComm, LPostCer(II)
75	Right Posterior Communicating Arte	RPostComm	0.4	0.0177	0.0177	RPostCer(I)	RDICAI
76	Left Posterior Communicating Arter	LPostComm	0.4	0.0177	0.0177	LPostCer(I)	LDICAI
77	Right Posterior Cerebral Artery II	RPostCer(II)	5.9	0.0314	0.0254	RPostCer(I)	VB:Brain
78	Left Posterior Cerebral Artery II	LPostCer(II)	5.9	0.0314	0.0254	LPostCer(I)	VB:Brain
79	Right Distal Internal Carotid Artery I	RDICA(I)	0.2	0.1195	0.1134	RICASin, RPostComm	RAntChor, RDICA(II)
80	Left Distal Internal Carotid Artery I	LDICA(I)	0.2	0.1195	0.1134	LIntCarSin, LPostComm	LAntChor, LDICA(II)
81	Right Anterior Cerebral Artery I	RAntCer(I)	1.2	0.0346	0.0314	RDICA(II)	RAntCer(II)
82	Left Anterior Cerebral Artery I	LAntCer(I)	1.2	0.0346	0.0314	LDICA(II)	AntComm, LAntCer(II)
83	Right Middle Cerebral Artery (M1)	RMCA(M1)	0.8	0.0707	0.0616	RDICA(II)	RMCAsup(M2), RMCAinf(M2)
84	Right Superior Middle Cerebral Arter	RMCAsup(M2)	7.1	0.0314	0.0314	RMCA(M1)	VB:Brain
85	Right Inferior Middle Cerebral Artery	RMCAinf(M2)	7.0	0.0314	0.0314	RMCA(M1)	VB:Brain
86	Left Middle Cerebral Artery (M1)	LMCA(M1)	0.8	0.0707	0.0616	LDICA(II)	LMCAsup(M2), LMCAinf(M2)
87	Left Superior Middle Cerebral Artery	LMCAsup(M2)	7.1	0.0314	0.0314	LMCA(M1)	VB:Brain
88	Left Inferior Middle Cerebral Artery (M	LMCAinf(M2)	7.0	0.0314	0.0314	LMCA(M1)	VB:Brain
89	Right Anterior Cerebral Artery II	RAntCer(II)	2.4	0.0254	0.0227	RAntCer(I), AntComm	VB:Brain
90	Anterior Communicating Artery	AntComm	0.2	0.0133	0.0133	LAntCer(I)	RAntCer(II)
91	Left Anterior Cerebral Artery II	LAntCer(II)	2.4	0.0254	0.0227	LAntCer(I)	VB:Brain
92	Right Internal Carotid Sinus	RICASin	1.1	0.1452	0.1195	RICA	RDICAI
93	Right Opthalmic Artery	ROpth	1.1	0.0079	0.0020	RICA	VB:Face/Neck
94	Left Internal Carotid Sinus	LIntCarSin	1.1	0.1452	0.1195	LICA	LDICAI
95	Left Opthalmic Artery	LOpth	1.1	0.0079	0.0020	LICA	VB:Face/Neck

Table 10: Physiological data for the 111 arteries from [10] (3).

96	Right External Carotid Artery II	RECA(II)	6.1	0.1257	0.0962	RECA(I)	RSupTemp, RMaxil
97	Right Superior Thyroid / Ascending Pharyngeal / Lingual / Facial / Occipital Arteries	RSupThy	10.1	0.0616	0.0616	RECA(I)	VB:Face/Neck
98	Left External Carotid Artery II	LExtCar(II)	6.1	0.1257	0.0962	LECA(I)	LSupTemp, LMaxil
99	Left Superior Thyroid / Ascending Pharyngeal / Lingual / Facial / Occipital Arteries	LSupThy	10.1	0.0380	0.0201	LECA(I)	VB:Face/Neck
100	Right Superior Temporal Artery	RSupTemp	6.1	0.0804	0.0707	RECA(II)	RSupTempFront, RSupTempPari
101	Right Maxillary Artery	RMaxil	9.1	0.0380	0.0079	RECA(II)	VB:Face/Neck
102	Left Superior Temporal Artery	LSupTemp	6.1	0.0804	0.0707	LExtCar(II)	LSupTempFront, LSupTempPari
103	Left Maxillary Artery	LMaxil	9.1	0.0380	0.0079	LExtCar(II)	VB:Face/Neck
104	Right Superior Temporal Frontal Art	RSupTempFront	10.0	0.0380	0.0154	RSupTemp	VB:Face/Neck
105	Right Superior Temporal Parietal Art	RSupTempPari	10.1	0.0380	0.0154	RSupTemp	VB:Face/Neck
106	Left Superior Temporal Frontal Arter	LSupTempFront	10.0	0.0380	0.0154	LSupTemp	VB:Face/Neck
107	Left Superior Temporal Parietal Arte	LSupTempPari	10.1	0.0380	0.0154	LSupTemp	VB:Face/Neck
108	Right Anterior Choroidal Artery	RAntChor	3.6	0.0177	0.0133	RDICAI	VB:Brain
109	Right Distal Internal Carotid Artery II	RDICA(II)	0.2	0.1134	0.1134	RDICAI	RAntCer(I), RMCA(M1)
110	Left Anterior Choroidal Artery	LAntChor	3.6	0.0177	0.0133	LDICAI	VB:Brain
111	Left Distal Internal Carotid Artery II	LDICA(II)	0.2	0.1134	0.1134	LDICAI	LAntCer(I), LMCA(M1)

D Stented artery, test case

Here we provide a test case with a stented artery, as originally presented in Rozendaal [7]. It provides insight into the basic workings of the model.

A stent is a metal or plastic tube inserted into the bloodstream to widen narrowed arteries to increase blood flow. The stent is generally stiffer than the surrounding blood vessel. We investigate the influence of the stent on the blood flow. To this end we model the stent as an increase in β with the same A_0. The stiffness is a factor of κ greater than that of the surrounding artery, β_0. A schematic overview is given in Figure 27. The blood vessel has a length l, from

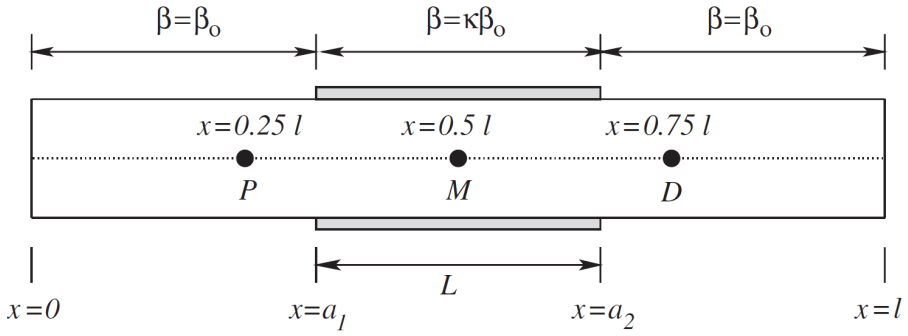

Figure 27: A schematic representation of an artery with a stent, from Sherwin et al.[15].

$x = a_1$ to $x = a_2$ a stent is placed with length L. At three points in the blood vessel the pressure is measured, P at $x = l/4$, M at $x = l/2$ and at $D = 3l/4$. The difference in β is made continuous using a C^1 continuous piecewise polynomial over a width of 2δ as is illustrated in Figure 28. All parameters are given in Table 11.

Table 11: Variables for the stented artery test case.

A_0 (cm^2)	l(cm)	a_1(cm)	a_2(cm)	L(cm)	ρ (g/cm^3)	δ(cm)	β_0 $(dyne/cm^2)$	$\kappa(-)$	T(s)
0.5	15	5	10	5	1	0.5	451352	100	0.33

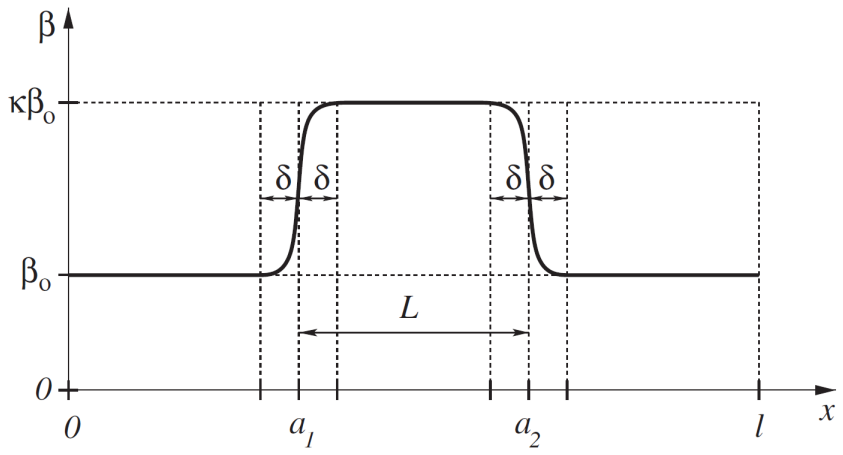

Figure 28: Variation of β, from Sherwin et al.[15].

D.1 Initial condition

As the initial condition, we choose a system completely at rest. This means that $A(t=0) = A_0$ and $u(t=0) = 0$. In vector form

$$U(x,0) = \begin{bmatrix} A(x,0) \\ u(x,0) \end{bmatrix} = \begin{bmatrix} 0.5 \\ 0 \end{bmatrix} \tag{101}$$

D.2 Boundary conditions

As discussed before, we need to describe boundary conditions at the inlet and outlet of the system. In this case there is one inlet and one outlet. At the inlet we prescribe pressure as

$$\bar{p}(t) = 20000 \sin\left(\frac{2\pi t}{T}\right) \mathrm{H}\left(\frac{T}{2} - t\right) \tag{102}$$

Where $H(t)$ denotes the Heaviside step function define as

$$H(t-a) = \begin{cases} 1 & t > a \\ 0 & t < a \end{cases} \tag{103}$$

In this case it allows half a sine period to pass. Using equation (14) we can write (102) as a condition for A

$$\bar{p} = p_{ext} + \beta(\sqrt{A} - \sqrt{A_0}) \Rightarrow A = \left(\frac{\bar{p}}{\beta} + \sqrt{A_0}\right)^2 \tag{104}$$

Where we have used that $p_{\mathrm{ext}} = 0$. Since we are using the forward prescription, we need to solve for w_1. Using (30) we get

$$w_1 = w_2 + 4\sqrt{\frac{2\beta}{\rho}} A^{1/4} \tag{105}$$

Fixing w_2 in its initial state and using (104) we arrive at

$$w_1(0,t) = w_2(0,0) + \frac{4\sqrt{2}}{\sqrt{\rho}} \sqrt{\bar{p}(t) + \beta_0 \sqrt{A_0}} \tag{106}$$

These values for w_1 and w_2 are used to calculate A and u using equation (30). A and u are then used as values for boundary ghost cell.

At the outlet we use a non-reflective boundary condition. This is achieved by

$$w_2(l,t) = w_2(l,0) = \text{ constant} \tag{107}$$

At $t = 0$ the system is at rest at $x = l$. This means there is no net left flowing wave. The boundary condition ensures that this is always the case. This leads to the boundary ghost cell being a copy of the last cell.

D.3 Stability

A grid of 400 cells is used. To ensure stability the CFL condition is met at each time t^n.

$$\Delta t^n = \frac{\Delta x}{|\lambda^n|_{\max}} \tag{108}$$

D.4 Results

We now compare results for a normal artery and a stented artery obtained by the flux difference splitting and the Discontinuous Galerkin as described in Sherwin et al. [15]. All variables for the normal artery are the same as the stented artery, only β is constant over the whole artery.

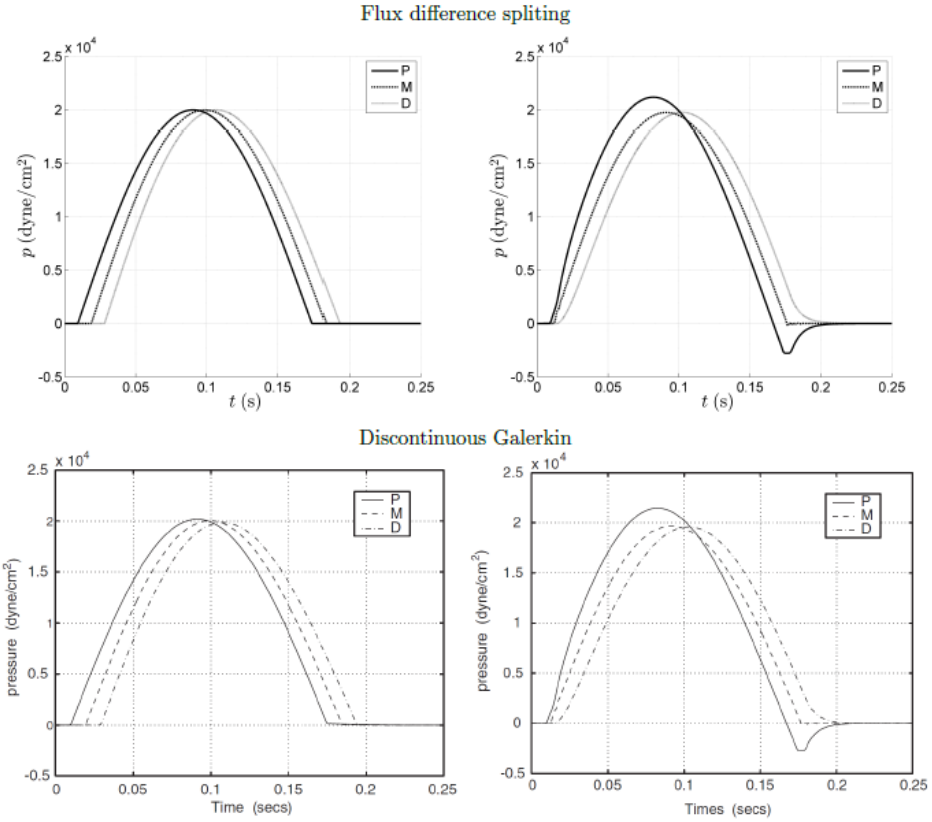

Figure 29: Results of the normal artery, left column, and the stented artery, right column. The top row contains results from the flux difference splitting, the bottom row contains results from the Discontinuous Galerkin method from Sherwin et al. [15].

The results from the normal artery shown in the left column show the half sine wave propagating non-distorted through the artery. There is no noticeable difference between the two methods.
The initial condition combined with the constant material properties ensures that w_1 and w_2 are constant at $t = 0$. Since the right boundary condition prescribes that w_2 is fixed at the outlet, w_2 is in fact constant for every x and t. This is consistent with a trivial constant solution for PDE (36). This also means that the wave speed $\lambda_1 = \frac{5w_1+3w_2}{8}$ does not depend on w_2. Thus the coupled quasi-linear system of PDEs decouples into two quasi-linear PDEs. Since w_1 is not constant in time it has a non trivial solution of its PDE. The small change in w_1, however, results in the quasi-linear effects being negligible. In fact, the difference in w_1 is at most 1 % and thus the difference in wave speed also at most 1%. The wave speed is large in comparison to the length of the artery ($\frac{\lambda_1}{l} \approx 100$). Thus the wave has long passed the end of the vessel when anything quasi-linear becomes noticeable.
Inserting a stent effectively splits the vessel into three domains, namely the vessel before the stent, the stent itself and the vessel after the stent. In each of these regions there are no sources and the model is governed by (36). Since the vessel is too short for quasi-linear effects to show, the model behaves as a scalar transport model. This means the shape of the wave is to a very good approximation preserved and the wave propagates through the vessel. In the stent, β is larger and thus λ_1 is also larger. Thus the points M and D are reached earlier by the pressure wave.

Figure 30: A 3D visualisation of the wave propagation through the normal artery, left, and the stented artery, right. Vessels are shown at $t = 0.01$s, $t = 0.075$s, $t = 0.175$s from left to right. The displacement from equilibrium is magnified by a factor 30. From [7].

There is a different situation at the boundaries of these models. There is a change in β. At the inlet $\frac{\partial \beta}{\partial x} > 0$, resulting in a positive source term for A. This results in the pressure increasing in P, this can be seen by the higher amplitude at P at $t = 0.08$s. At the outlet, the situation is reversed and we get a negative left running wave, this can be seen at P at $t = 0.18$s.

Overall, the flux difference splitting method produces comparable results to the Discontinuous Galerkin. There are differences though, as can be seen in the slightly lower peak pressure at P in the stented artery. This difference is minute however. In Figure 30 there is a 3D visualisation of the wave propagation from [7].

For more single artery test cases comparing the flux difference method and the Discontinuous Galerkin the reader is referred to [7]. They look at an abnormal long artery to investigate non-linearity and a tapered artery. In general it is shown that the two methods produce very similar results.